Monthly Notices
of the
ROYAL ASTRONOMICAL SOCIETY

Mon. Not. R. Astron. Soc. **422,** 1999–2023 (2012) doi:10.1111/j.1365-2966.2012.20623.x

Sunyaev–Zel'dovich clusters in Millennium gas simulations

Scott T. Kay,[1⋆] Michael W. Peel,[1] C. J. Short,[2] Peter A. Thomas,[2] Owain E. Young,[2] Richard A. Battye,[1] Andrew R. Liddle[2] and Frazer R. Pearce[3]

[1]*Jodrell Bank Centre for Astrophysics, School of Physics and Astronomy, The University of Manchester, Manchester M13 9PL*
[2]*Astronomy Centre, Department of Physics and Astronomy, University of Sussex, Brighton BN1 9QH*
[3]*Department of Physics and Astronomy, University of Nottingham, Nottingham NG7 2RD*

Accepted 2012 January 24. Received 2012 January 23; in original form 2011 December 15

ABSTRACT

Large surveys using the Sunyaev–Zel'dovich (SZ) effect to find clusters of galaxies are now starting to yield large numbers of systems out to high redshift, many of which are new discoveries. In order to provide theoretical interpretation for the release of the full SZ cluster samples over the next few years, we have exploited the large-volume Millennium gas cosmological N-body hydrodynamics simulations to study the SZ cluster population at low and high redshift, for three models with varying gas physics. We confirm previous results using smaller samples that the intrinsic (spherical) Y_{500}–M_{500} relation has very little scatter ($\sigma_{\log_{10} Y} \simeq 0.04$), is insensitive to cluster gas physics and evolves to redshift 1 in accordance with self-similar expectations. Our *preheating* and *feedback* models predict scaling relations that are in excellent agreement with the recent analysis from combined *Planck* and *XMM–Newton* data by the Planck Collaboration. This agreement is largely preserved when r_{500} and M_{500} are derived using the hydrostatic mass proxy, $Y_{\rm X,500}$, albeit with significantly reduced scatter ($\sigma_{\log_{10} Y} \simeq 0.02$), a result that is due to the tight correlation between Y_{500} and $Y_{\rm X,500}$. Interestingly, this assumption also hides any bias in the relation due to dynamical activity. We also assess the importance of projection effects from large-scale structure along the line of sight, by extracting cluster Y_{500} values from 50 simulated 5×5-deg^2 sky maps. Once the (model-dependent) mean signal is subtracted from the maps we find that the integrated SZ signal is unbiased with respect to the underlying clusters, although the scatter in the (cylindrical) Y_{500}–M_{500} relation increases in the *preheating* case, where a significant amount of energy was injected into the intergalactic medium at high redshift. Finally, we study the hot gas pressure profiles to investigate the origin of the SZ signal and find that the largest contribution comes from radii close to r_{500} in all cases. The profiles themselves are well described by generalized Navarro, Frenk & White profiles but there is significant cluster-to-cluster scatter. In conclusion, our results support the notion that Y_{500} is a robust mass proxy for use in cosmological analyses with clusters.

Key words: hydrodynamics – methods: numerical – galaxies: clusters: general – X-rays: galaxies: clusters.

1 INTRODUCTION

The Sunyaev–Zel'dovich (SZ) effect (Sunyaev & Zel'dovich 1972) is a powerful method for discovering new clusters of galaxies. It arises generically due to the scattering of cosmic microwave background (CMB) photons off free electrons, leading to a predictable spectral distortion in the CMB, that is, in the non-relativistic limit, linearly dependent on the line integral of the electron pressure (Birkinshaw 1999). In modern theories of structure formation, the dominant contribution to the SZ signal comes from the intracluster medium (ICM), a diffuse plasma within clusters that is approximately in hydrostatic equilibrium (HSE) within the dark matter dominated potential (see Voit 2005; Allen, Evrard & Mantz 2011 for recent reviews). The key SZ observable is the Y parameter, defined as

$$Y = \int y \, {\rm d}\Omega, \tag{1}$$

where the integral is performed over the solid angle subtended by the cluster. The Compton-y parameter is determined by the thermal

⋆E-mail: Scott.Kay@manchester.ac.uk

structure of the ICM:

$$y = \frac{\sigma_{\rm T} k}{m_{\rm e} c^2} \int n_{\rm e} T_{\rm e} \, {\rm d}l, \quad (2)$$

where $n_{\rm e}$ and $T_{\rm e}$ are the density and temperature of the free electrons, respectively, and dl is the differential line element along the line of sight. Since Y can be expressed as a volume integral of the pressure (when the redshift and cosmological parameters are specified), it measures the total thermal energy of the gas, a property that ought to be strongly correlated with the cluster's mass through the virial theorem. This means that Y ought to be relatively insensitive to the complex microphysics taking place in the cluster core, unlike other global properties such as X-ray luminosity.

Early observational studies confirmed the detection of an SZ signal towards known massive clusters of galaxies and used this to estimate the Hubble constant (e.g. Jones et al. 1993; Birkinshaw & Hughes 1994). Over the past decade, SZ observations of known bright X-ray bright clusters have become routine, allowing the investigation of cluster scaling relations to be performed (e.g. McCarthy et al. 2003b; Benson et al. 2004; Morandi, Ettori & Moscardini 2007; Bonamente et al. 2008; Huang et al. 2010; Lancaster et al. 2011; Shimwell et al. 2011). One potential shortcoming of this approach is that the samples are X-ray selected and therefore biased towards luminous, cool-core systems at low redshift.

In the past few years, SZ science has entered the exciting new phase of blind surveys, where detections of new clusters have become possible (Staniszewski et al. 2009). Indeed, SZ surveys are now yielding large numbers of SZ-selected clusters, many of them new detections, especially from the South Pole Telescope (SPT; Vanderlinde et al. 2010; Andersson et al. 2011; Williamson et al. 2011), the Atacama Cosmology Telescope (ACT; Marriage et al. 2011; Sehgal et al. 2011) and the *Planck* satellite (Ade et al. 2011a,b, c). Since the SZ effect is effectively independent of redshift, the SZ selection function tends to favour higher redshift systems than the X-ray counterpart, assuming similar angular resolution. As a result, the new blind SZ surveys are starting to find new massive systems at $z \sim 1$ (Ade et al. 2011d; Foley et al. 2011; Menanteau et al. 2012). In the near future, we should expect to see these numbers increase substantially as the full survey results are published, nicely complementing X-ray surveys such as the MAssive Cluster Survey (MACS; Ebeling, Edge & Henry 2001) and the XMM Cluster Survey (XCS; Romer et al. 2001; Mehrtens et al. 2011). Such complementarity will be further exploited with the next generation of X-ray surveys (e.g. with *eROSITA*) and millimetric telescopes (e.g. CCAT; see Golwala et al. 2009).

One of the main goals of SZ surveys is to measure cosmological parameters (e.g. Barbosa et al. 1996; Carlstrom, Holder & Reese 2002; Battye & Weller 2003). Central to the cosmological application of SZ surveys is the scaling relation between the observables (Y and redshift, z) and cluster mass, M. Under the assumption that clusters form a self-similar population (Kaiser 1986) the SZ flux should scale as $Y \propto M^{5/3} H(z)^{2/3}$, when measured within a radius enclosing a mean density that is a constant multiple of the critical density of the Universe. Early theoretical studies combined such simple scaling relations with the Press–Schechter formalism (Press & Schechter 1974) to predict the SZ evolution of the cluster population in a variety of cosmological models (e.g. Cole & Kaiser 1988; Bartlett & Silk 1994; Barbosa et al. 1996; Eke, Cole & Frenk 1996; Aghanim et al. 1997; Kay, Liddle & Thomas 2001; Battye & Weller 2003). More recently, attention has turned to more detailed studies of how cluster gas physics impacts upon SZ scaling relations, both using semi-analytic models (e.g. McCarthy et al. 2003a,b; Shaw, Holder & Bode 2008) and full cosmological N-body/hydrodynamic simulations (da Silva et al. 2000; White, Hernquist & Springel 2002; da Silva et al. 2004; Motl et al. 2005; Nagai 2006; Bonaldi et al. 2007; Hallman et al. 2007; Aghanim, da Silva & Nunes 2009; Battaglia et al. 2011). Simulations are now also being used to investigate the effects of mergers on SZ scaling relations (Poole et al. 2007; Wik et al. 2008; Yang, Bhattacharya & Ricker 2010; Krause et al. 2012). A generic result from these studies is that the self-similar description appears to be approximately valid on cluster scales ($M > 10^{14}\, h^{-1}\, {\rm M}_{\odot}$) but in detail differences are seen between the models that are due to the effects of non-gravitational physics (cooling and heating processes), especially at low mass where the gas fraction is depleted.

Two of the main shortcomings in previous simulation studies are the relatively small samples (that are sometimes restricted to lower mass clusters) and a limited range of (uncertain) cluster gas physics models, often not calibrated to match X-ray data. Some studies may satisfy one of these criteria but usually not both. A new generation of simulations are now starting to overcome both shortcomings. Stanek et al. (2010) recently presented results from two of the *Millennium gas* simulations (MGSs; Hartley et al. 2008), large-volume runs based on the Millennium simulation (MS; Springel et al. 2005) with varying gas physics. These simulations are sufficiently large to enable the full range of cluster masses (10^{14}–$10^{15}\, h^{-1}\, {\rm M}_{\odot}$) to be studied and one of the runs, where the gas was preheated at high redshift, is able to match the mean X-ray luminosity–temperature relation at $z = 0$ (Hartley et al. 2008). Although the work of Stanek et al. (2010) was focused on the more general issue of multivariate scaling relations, they presented results for the SZ Y–M relation measured within a radius corresponding to a mean internal density equal to 200 times the critical density, r_{200}.

The aim of this paper is to use these MGSs to focus in more detail on predictions of the SZ effect and, in particular, the Y–M relation for clusters. Our paper builds on the Stanek et al. (2010) work in three important ways. First, we add a third model that includes a more realistic treatment of feedback, both from supernovae and active galactic nuclei (AGNs). This model has already been shown to successfully match many of the X-ray properties of non-cool core clusters (Short & Thomas 2009; Short et al. 2010). Secondly, we include in our analysis simulated maps of the full SZ effect along the line of sight, to assess the projection effects of large-scale structure. Finally, we attempt to produce results for our Y–M scaling relations using methods that are more closely matched with observations. In particular, we present our results for the smaller r_{500} and investigate the impact of assuming HSE and a mass proxy ($Y_{\rm X}$, Kravtsov, Vikhlinin & Nagai 2006) on the Y–M relation.

We organize the remainder of this paper as follows. In Section 2, we outline the simulation details and our methods used to define cluster properties. We also present some basic properties of the sample and SZ maps. Sections 3, 4 and 5 contain our main results: in Section 3 we present an analysis of the hot gas pressure profiles, before going on to study SZ scaling relations in Section 4 and the impact of hydrostatic bias in Section 5. Finally, in Section 6 we summarize our main conclusions and outline future work.

2 SIMULATION DETAILS

Our results are drawn from the MGSs, a set of large, cosmological hydrodynamics simulations of the Λ cold dark matter cosmology ($\Omega_{\rm m} = 0.25$, $\Omega_{\Lambda} = 0.75$, $\Omega_{\rm b} = 0.045$, $h = 0.73$, $\sigma_8 = 0.9$). In this section, we summarize the details of these simulations and present

our methods for constructing simulated cluster properties and SZ sky maps.

2.1 Millennium gas simulations

The MGSs (see Hartley et al. 2008; Stanek, Rudd & Evrard 2009; Short et al. 2010; Stanek et al. 2010; Young et al. 2011) were constructed to provide hydrodynamic versions of the Virgo Consortium's dark matter MS (Springel et al. 2005). The simulations were therefore started from the same realization of the large-scale density field within the same comoving box-size, $L = 500\,h^{-1}$ Mpc, and used the same set of cosmological parameters. The MGSs were run with the publicly available GADGET2 N-body/hydrodynamics code (Springel 2005). Due to the increased computational requirements from the inclusion of gas particles, the simulations were run with fewer (5×10^8 each of gas and dark matter) particles in total than the MS. The particle masses were therefore set to $m_{\rm gas} = 3.1 \times 10^9\,h^{-1}\,{\rm M}_\odot$ and $m_{\rm dm} = 1.4 \times 10^{10}\,h^{-1}\,{\rm M}_\odot$ for the gas and dark matter, respectively. Gravitational forces were softened at small separations using an equivalent Plummer softening length of $\epsilon = 100\,h^{-1}$ kpc, held fixed in comoving coordinates. At low redshift ($z < 3$) the softening was then fixed to $\epsilon = 25\,h^{-1}$ kpc in physical coordinates.

Two versions of the MGSs were run with the above properties. Both runs started from identical initial conditions but differed in the way the gas was evolved. In the first run, the gas was modelled as an ideal non-radiative fluid. In addition to gravitational forces, the gas could undergo adiabatic changes in regions of non-zero pressure gradients, modelled using the smoothed particle hydrodynamics (SPH) formalism (see Springel & Hernquist 2002 for the version of SPH used in GADGET2). Additionally, in regions where the flow was convergent the bulk kinetic energy of the gas is converted into internal energy using an artificial viscosity term; this is essential to capture shocks and thus generate quasi-hydrostatic atmospheres within virialized dark matter haloes. In accordance with previous studies (e.g. Short et al. 2010), we refer to this simulation as the *gravitation-only* (GO) model.

It is well known that a non-radiative description of intracluster gas does not agree with the observed X-ray properties of clusters, especially at low masses, where an excess of core entropy is required to produce a steeper X-ray luminosity–temperature relation (e.g. Voit 2005). A simple method capable of generating this excess entropy is to *preheat* the gas at high redshift before cluster collapse (Evrard & Henry 1991; Kaiser 1991). We implemented this method in a second simulation by raising the minimum entropy[1] of the gas (by increasing its temperature) to $K_{\rm min} = 200\,{\rm keV\,cm^2}$ at $z = 4$. The entropy level was chosen so as to match the mean $z = 0$ X-ray luminosity–temperature relation (Hartley et al. 2008). We also included radiative cooling, an entropy sink. However, this made very little difference, as the cooling time of the preheated gas is very long compared to the Hubble time and therefore gas could no longer cool and form stars before the end of the simulation. We refer to this simulation using the label PC, for *preheating plus cooling*.

We also consider a third model when analysing the SZ properties from individual clusters. This is the *feedback-only* (FO) model developed by Short & Thomas (2009) and then applied to MGS clusters by Short et al. (2010), where full details of the method may be found. Briefly, it uses the semi-analytic galaxy formation model of De Lucia & Blaizot (2007), run on dark matter only resimulations of MS clusters, to provide information on the effects of star formation and feedback on the intracluster gas. The model works as follows. Galaxy merger trees are first generated by applying the semi-analytic model to the dark matter distribution. Various properties of the galaxies (such as their position, stellar mass and black hole mass) are stored at each snapshot of the simulation. The clusters are then resimulated with gas, assuming that the gas particles have zero gravitational mass; this guarantees that the dark matter distributions (and therefore galaxy positions) are identical to those in the parent dark matter only simulation. At each snapshot time, two important changes are made to the gas. First, the increase in stellar mass of each cluster galaxy is used to convert local intracluster gas into stars, a requirement for generating sensible stellar and gas fractions (Young et al. 2011). This change in stellar mass is also used to heat the gas from supernova explosions. Secondly, any increase in black hole mass is used to heat the gas on the basis that such accretion leads to an AGN. The heating rate, known as AGN feedback, is taken from Bower, McCarthy & Benson (2008) and is given by

$$\dot{E}_{\rm feed} = \min\left(\epsilon_{\rm SMBH} L_{\rm Edd}, \epsilon_{\rm r} \dot{M}_{\rm BH} c^2\right), \quad (3)$$

where $\epsilon_{\rm SMBH} = 0.02$ dictates the maximum heating rate (in units of the Eddington luminosity) and $\epsilon_{\rm r} = 0.1$ is the efficiency with which the accreted mass is converted into feedback energy. This is particularly important because AGNs are the dominant feedback mechanism on cluster scales.

We analyse the same sample of 337 clusters studied by Short et al. (2010), comprising all objects in the MS with virial mass $M_{\rm vir} > 5 \times 10^{14}\,h^{-1}\,{\rm M}_\odot$ and a random sample at lower mass ($1.7 \times 10^{13} \leq M_{\rm vir} \leq 5 \times 10^{14}\,h^{-1}\,{\rm M}_\odot$) chosen such that there were a fixed number of objects within each logarithmic mass bin. The FO model successfully generates the required excess entropy of the low-redshift population and provides a good match to the structural properties of non-cool-core clusters. The main shortcoming of this model is that it neglects the effects of radiative cooling and therefore cannot reproduce the most X-ray luminous cool-core population (Short et al. 2010). This failure may not be as serious as it seems, however, since there is some evidence that the X-ray cool-core population diminishes with increasing redshift, both from observations (e.g. Maughan et al. 2012) and from simulations (e.g. Kay et al. 2007). Furthermore, as we will demonstrate, the SZ Y parameter (which measures the global thermal energy of the intracluster gas) is reasonably insensitive to changes in gas physics that predominantly affect the cluster core. Issues relevant to this study where cooling could impact upon our results are the degree to which the ICM is hydrostatic and the effect of gas clumping on the X-ray quantity, $Y_{\rm X}$, used as a cluster mass proxy. We note that a first step towards including radiative cooling in the model has been made and shows promising results (Short, Thomas & Young 2012). Ultimately, a fully self-consistent scheme is desirable, where the same cooling and heating rates are used in both the semi-analytic model and hydrodynamic simulation.

2.2 Cluster definitions and estimation of global properties

Clusters are defined in exactly the same way as in Kay et al. (2007). First, a Friends-of-Friends code is run on the dark matter particles for each snapshot. The dimensionless linking length (in units of the mean interparticle separation) is set to $b = 0.1$, chosen to minimize the probability of linking two haloes together outside their respective virial radii. The dark matter particle with the most negative

[1] In the usual way, we take entropy to mean the quantity $K = kT/n_{\rm e}^{2/3}$, where T is the gas temperature and $n_{\rm e}$ is the free electron density.

gravitational potential energy is then identified for each group and this is taken to be the centre.

In the next stage, a sphere is centred on each Friends-of-Friends group and its radius increased until the total mass (from dark matter, gas and stars, when present) satisfies

$$M_\Delta = \frac{4\pi}{3} r_\Delta^3 \Delta \rho_{\rm cr}(z), \tag{4}$$

where r_Δ is the proper radius of the sphere, Δ is a specified density contrast, $\rho_{\rm cr}(z) = (3H_0^2/8\pi G)E(z)^2$ is the critical density and $E(z)^2 = \Omega_{\rm m}(1+z)^3 + \Omega_\Lambda$ for a flat universe. We assume $\Delta = 500$ for the main results in this study as this value is commonly adopted for observational studies (some of which we will compare to) because r_{500} is sufficiently large to make many integrated properties insensitive to variations in core structure, while also being small enough to be within reach for detailed X-ray observations of many objects. We occasionally use the value of Δ appropriate for the virial radius, $r_{\rm vir}$, as defined by the spherical top-hat collapse model. This is a redshift-dependent quantity, $\Delta = \Delta_{\rm c}(z)$, which we calculate using the fitting formula given by Bryan & Norman (1998). Note that at $z = 0$, $\Delta_{\rm c} \simeq 94$ and $r_{\rm vir} \simeq 2\, r_{500}$.

Once the cluster's mass and radius is defined, we calculate various properties of the hot gas, the most important being the SZ flux. The frequency-independent part is given by

$$Y_{500} = \frac{1}{D_{\rm A}^2} \frac{\sigma_{\rm T}}{m_{\rm e}c^2} \int n_{\rm e} k T_{\rm e}\, {\rm d}V, \tag{5}$$

where $D_{\rm A}$ is the (cosmology-dependent) angular diameter distance from the cluster and the integral is performed over the entire cluster sphere. To simplify matters, we redefine the integrated SZ Y parameter

$$Y_{500}\, D_{\rm A}^2 \rightarrow Y_{500}, \tag{6}$$

since this combination is directly proportional to the integrated thermal energy of the gas which is the physical property of interest. Note that the dimensions of Y_{500} are now that of area; we will therefore present values in $h^{-2}\,{\rm Mpc}^2$ units. The value of Y_{500} is estimated for each cluster using

$$Y_{500} = \left(\frac{\sigma_{\rm T} k m_{\rm gas}}{\mu_{\rm e} m_{\rm H} m_{\rm e} c^2} \right) \sum_{i=1}^{N_{\rm hot}} T_i, \tag{7}$$

where the sum runs over all hot ($T > 10^5$K) gas particles within r_{500}, with mass $m_{\rm gas}$ and temperature T_i. We adopt the value $\mu_{\rm e} = 1.14$ for the mean molecular weight per free electron, appropriate for a fully ionized plasma of hydrogen (with mass fraction $X = 0.76$) and helium (with mass fraction $Y = 1 - X$). We also assume equipartition of energy between the electrons and nuclei; thus, $T = T_{\rm e}$.

We estimate the X-ray temperature of the ICM using the spectroscopic-like temperature $T_{\rm sl}$ (Mazzotta et al. 2004), appropriate for bremsstrahlung in hot ($kT > 3\,{\rm keV}$) clusters,

$$T_{\rm sl} = \frac{\sum_{i=1}^{N_{\rm hot}} \rho_i T_i^{1/4}}{\sum_{i=1}^{N_{\rm hot}} \rho_i T_i^{-3/4}}, \tag{8}$$

where ρ_i is the density of particle i and in this case the sum runs over all hot gas particles with $kT_i > 0.5$keV. We measure $T_{\rm sl}$ in the region outside the cluster core ($x_{\rm core} < r/r_{500} < 1$, where $x_{\rm core} = 0.1$ for the GO and PC models, and 0.15 for the FO model[2]) to provide a closer match to observed X-ray temperature measurements (where a larger variation in core temperature is seen than in our simulations).

A quantity related to Y_{500} is $Y_{\rm X,500} \propto M_{\rm gas} T_{\rm X}$, estimated from X-ray data. Introduced by Kravtsov et al. (2006), it was shown to be a low-scatter proxy for cluster mass (due to scatter in X-ray temperature being negatively correlated with scatter in gas mass). We estimate this quantity as

$$Y_{\rm X,500} = \left(\frac{\sigma_{\rm T} k}{\mu_{\rm e} m_{\rm H} m_{\rm e} c^2} \right) M_{\rm gas,500}\, T_{\rm sl}, \tag{9}$$

where $M_{\rm gas,500}$ is the mass of hot gas within r_{500}, although we occasionally present $Y_{\rm X,500}$ in its native ($h^{-1}\,{\rm M}_\odot\,{\rm keV}$) units, that is, simply assuming $Y_{\rm X,500} = M_{\rm gas,500} k T_{\rm sl}$. The main difference between Y and $Y_{\rm X}$ is that the former depends on the mass-weighted temperature, while the latter depends on the X-ray temperature, which is more heavily weighted by lower entropy gas (Mazzotta et al. 2004). Comparing Y with $Y_{\rm X}$ therefore implicitly tests the *clumpiness* of the ICM since clumpy gas will be cooler and therefore have lower X-ray temperature relative to the mass-weighted temperature (e.g. Kay et al. 2008). As we show below, this effect is model-dependent but is of minimal importance in the PC and FO simulations.

Table 1. Number of clusters in our samples at redshifts $z = 0$, 0.5 and 1. Column 1 gives the model label and column 2 the redshift. Column 3 lists the total number of clusters in each sample with $M_{500} > 10^{14}\, h^{-1}\,{\rm M}_\odot$, while columns 4 and 5 subdivide the sample into *regular* and *disturbed* populations, respectively, using the s parameter defined in equation (10).

Model	Redshift	$N_{\rm clus}$	$N_{\rm clus}\,(s \leq 0.1)$	$N_{\rm clus}\,(s > 0.1)$
GO	0.0	1110	986	124
	0.5	567	457	110
	1.0	139	103	36
PC	0.0	883	799	84
	0.5	436	355	81
	1.0	102	78	24
FO	0.0	188	154	34
	0.5	148	122	26
	1.0	75	51	24

2.3 Cluster sample

Table 1 summarizes the number of clusters in each of the runs at redshifts $z = 0$, 0.5 and 1. For our fiducial sample we have employed a lower mass cut of $M_{500} > 10^{14}\, h^{-1}\,{\rm M}_\odot$, a useful limit for comparing with SZ cluster data. The GO and PC simulations have similar numbers, although the latter is slightly smaller due to the effect of preheating on the gas fraction (Stanek et al. 2009). Note the number of clusters at $z = 1$ is around an order of magnitude lower than at $z = 0$. There are significantly fewer FO clusters at any given redshift due to the fact that it is not a volume-limited sample. The drop in number at high redshift is not as severe in this case as the mean mass of the sample is higher and so a smaller fraction of clusters drop below the imposed mass limit.

We also consider the effect of ongoing mergers by splitting our sample into *regular* and *disturbed* subsamples, using a simple estimator known as the *substructure statistic* (Thomas et al. 1998; Kay

[2] The GO/PC and FO data were processed independently and different choices for $x_{\rm core}$ were made at those times. However, the effect of this difference on $T_{\rm sl}$ is small; we checked by recalculating the GO/PC temperatures at $z = 0$ using $x_{\rm core} = 0.15$ and found only a 2–3 per cent increase, on average.

et al. 2007), defined as

$$s = \frac{|\boldsymbol{r}_\phi - \boldsymbol{r}_{\rm cm}|}{r_{500}}, \tag{10}$$

where $\boldsymbol{r}_\phi$ is the position of the cluster centre (defined here to be the position of the dark matter particle with the most negative potential, ϕ) and $\boldsymbol{r}_{\rm cm}$ is the centre-of-mass. We define those clusters with $s > 0.1$ as disturbed systems and those with $s \leq 0.1$ as regular systems, although note that this terminology is strictly for convenience as all clusters are disturbed to some degree. In practice, this value delineates those that are clearly undergoing significant mergers, as discussed in Kay et al. (2007). The fraction of disturbed clusters increases with redshift in all models, from around 10 per cent at $z = 0$ to 25 per cent at $z = 1$, in the GO and PC models. Again, the different method for cluster selection in the FO model modifies the result but nevertheless the trend of increasing disturbed fraction with redshift is still seen.

2.4 Cluster profiles

We discuss hot gas pressure profiles in Section 3 as these are important for understanding the relative contribution to the SZ signal from different radii. The profiles are constructed by first identifying all hot gas particles within a radius r_{500} of the cluster centre. This sphere is then sub-divided into spherical shells with fixed radial thickness in $\log_{10}(x)$, where $x = r/r_{500}$. The pressure within the shell is then estimated using a mass-weighted average

$$P(x) = \frac{1}{V(x)} \frac{k}{\mu m_{\rm H}} \sum_{i=1}^{N_{\rm shell}} m_i T_i, \tag{11}$$

where the sum runs over all hot gas particles within the shell at radial position x, V is the volume of the shell and $\mu = 0.59$ is the mean molecular weight for an ionized plasma (assuming zero metallicity).

2.5 Cluster maps

We also compute the thermal SZ effect due to an individual cluster by constructing Compton-y maps. This allows us to separate the cluster contribution (within a cylinder) from the total integrated signal along the line of sight. Each map is constructed by first identifying all hot gas particles within a cuboid of size $2r_{\rm vir} \times 2r_{\rm vir} \times 6r_{\rm vir}$, centred on the cluster. The particles are then projected along the long axis of the cuboid and smoothed on to a 2D grid, creating the y distribution. We estimate y at the location of each pixel, $\boldsymbol{R}_{\rm p} = (x, y)$, as

$$y(\boldsymbol{R}_{\rm p}) = \frac{\sigma_{\rm T} k m_{\rm gas}}{A_{\rm pix} \mu_{\rm e} m_{\rm H} m_{\rm e} c^2} \sum_i \frac{w(|\boldsymbol{R}_i - \boldsymbol{R}_{\rm p}|, h_i) T_i}{\sum_{\rm p} w(|\boldsymbol{R}_i - \boldsymbol{R}_{\rm p}|, h_i)}, \tag{12}$$

where $A_{\rm pix}$ is the area of a single pixel and w is the projected version of the SPH kernel used by GADGET2. The main sum runs over all hot gas particles with projected position $\boldsymbol{R}_i$, temperature T_i and SPH smoothing length h_i. The sum in the denominator runs over all pixels and normalizes the kernel for each particle.

Fig. 1 illustrates Compton-y maps for two massive clusters in our simulations at $z = 0$: a regular ($s \simeq 0.02$) cluster with a virial mass $M_{\rm vir} \simeq 2.9 \times 10^{15}\, h^{-1}\, {\rm M}_\odot$ (the most massive object in the MS) and a merging ($s \simeq 0.1$) cluster with $M_{\rm vir} \simeq 1.5 \times 10^{15}\, h^{-1}\, {\rm M}_\odot$. The left-hand panels show results for the GO simulation, the middle panels for the PC simulation and the right-hand panels for the FO simulation.

As has been seen in previous simulations (e.g. Motl et al. 2005), the y distribution is very smooth. The most significant features are sharp edges associated with shocks; this is especially clear in the case of the merging cluster. Qualitatively, the maps look structurally similar between models although their y values within a given pixel can be significantly different, with the GO and PC models lying at either extreme. For the regular GO cluster, the mean y within the virial radius is $\langle y \rangle = 1.4 \times 10^{-5}$, with a range of values from 2×10^{-7} to 7×10^{-4}. For the PC cluster, the mean value is very similar although the maximum y (associated with the centre of the cluster) is almost half ($y_{\rm max} = 4 \times 10^{-4}$). This is due to the preheating of the gas which acts to smooth out the high-density regions.

It is also noticeable that the GO clusters contain a significant amount of small-scale structure in the gas. This is not clear in the y distribution but is evident from the overlaid X-ray surface brightness contours.[3] These are clumps of low-entropy gas associated with substructures in the cluster. Again, the preheating has smoothed these out by raising the entropy of the gas at high redshift. These features are also seen in the FO clusters, where heating is localized to haloes in which AGN feedback is occurring.

2.6 Sky maps

We also analyse simulated sky maps of the thermal SZ effect for the GO and PC models, using the *stacked box* approach pioneered by da Silva et al. (2000). This is an approximate method for generating past light cones using a finite number of outputs. To do this we first compute the look-back time corresponding to a comoving distance of $50\, h^{-1}$ Mpc. We then calculate successive look-back times increasing the comoving distance in steps of $\Delta_{\rm map} = 100\, h^{-1}$ Mpc. These look-back times are used to find the nearest output time when simulation data are stored (a total of 160 snapshots were generated). We also calculate the comoving width required at each look-back time, corresponding to a fixed opening angle of $\theta_{\rm map} = 5^\circ$. The final look-back time is chosen such that the comoving width is still smaller than the box size, to avoid replication of the particles. The choice of $\theta_{\rm map}$ allows us to integrate the SZ effect out to a maximum redshift, $z_{\rm max} = 4.7$, using 47 snapshots; this is sufficiently large for the mean y signal to be converged in our simulations (see Fig. 3, discussed below).

Once the required volumes are defined to make up the light cone, the second stage is to use a random number generator to construct a table of random translations, rotations (in steps of $\pi/2$ radians) and reflections about each of the three axes. This is done in order to minimize the chance of the light cone containing the same cluster at different redshifts (note the volume required at each time is always less than 20 per cent of the full simulation box because of our choice of $\Delta_{\rm map}$). The list of operations is then used to determine which particles are required to compute the contribution to the SZ signal from each redshift (used to create a so-called *partial* map). This stage is repeated 50 times to allow us to generate 50 quasi-independent realizations.

The final stage is to generate the partial maps themselves, by smoothing the appropriate gas particles on to a 2D grid. This is done using the same technique as for individual clusters but now using a

[3] X-ray surface brightness maps are calculated by replacing T_i in equation (12) with $\rho_i \Lambda(T_i, Z)$, where ρ_i is the density of hot gas particle i and $Z = 0.3\, {\rm Z}_\odot$ is the assumed metallicity. The cooling function, $\Lambda(T, Z)$, is calculated for the soft [0.5–2] keV band. We normalize each surface brightness map to the maximum pixel value.

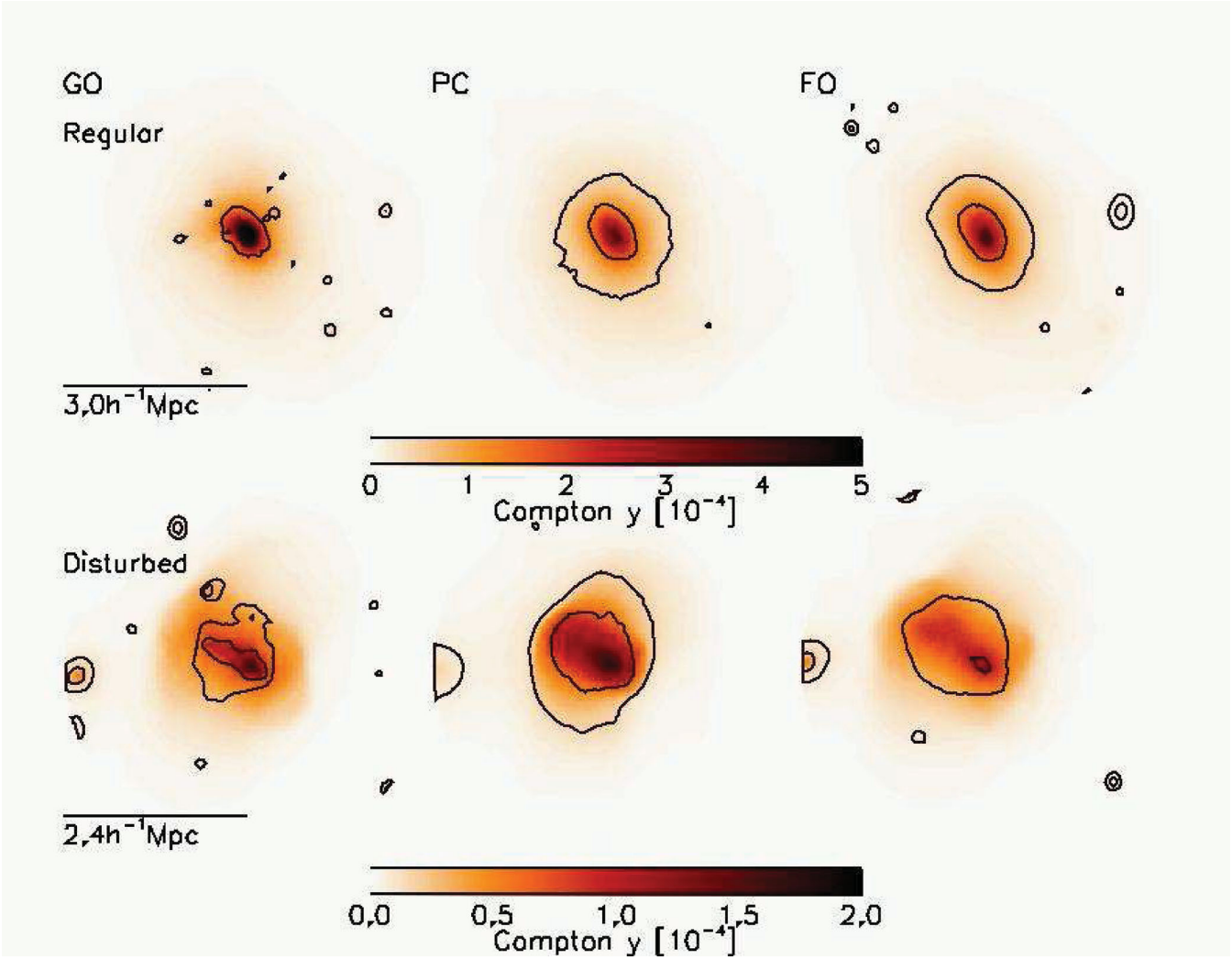

Figure 1. Top panels: Compton-y maps for the most massive cluster at $z = 0$ in the MS ($M_{\rm vir} \simeq 2.9 \times 10^{15}\,h^{-1}\,{\rm M}_{\odot}$, which we classify as regular) with X-ray surface brightness contours overlaid. Results are shown, from the left-hand to right-hand side, for the cluster in the GO, PC and FO models, respectively. Images in the bottom panels are similar except a massive disturbed cluster (with $M_{\rm vir} \simeq 1.5 \times 10^{15}\,h^{-1}\,{\rm M}_{\odot}$) is shown. Each panel is $2r_{\rm vir}$ across and the scale and value of $r_{\rm vir}$ are shown in the left-hand panels. The range of y values is given for each cluster in the scale at the bottom of each row; note the disturbed cluster has a lower maximum value than the regular cluster. The X-ray contours illustrate levels that are 10 and 1 per cent of the maximum value in the map. The gross features are similar in all three models for both clusters, although the X-ray maps reveal that the gas in the PC clusters is the smoothest, while the GO clusters contain gas with the most small scale structure.

map area corresponding to $\theta_{\rm map} \times \theta_{\rm map}$ at each redshift and a comoving depth of $\Delta_{\rm map}$. Each partial map contains 1200×1200 pixels such that each pixel has an angular size, $\theta_{\rm pix} = 0.25$ arcmin, comfortably smaller than the typical resolution of current SZ telescopes (1–10 arcmin). The 47 partial maps are then stacked for each realization to make final maps of the y parameter.

Fig. 2 shows an example Compton-y sky map for realization 46, chosen because it contains a relatively large cluster. Both the GO (left-hand panel) and PC (right-hand panel) versions are shown. The maps were smoothed using a Gaussian kernel with a full width at half-maximum of 1 arcmin, similar to the resolution of modern ground-based SZ telescopes such as SPT and ACT.

The most striking difference between the two maps is the contrast: the PC map has a higher background than the GO map, making it harder to visually pick out the SZ sources associated with the clusters. This is due to the extra thermal energy added to *all* the gas by the preheating process and can be quantified by measuring the mean y parameter, averaged over all 50 realizations. For the GO run, we find $\langle y \rangle = 2.3 \times 10^{-6}$, increasing by more than a factor of 4 to $\langle y \rangle = 9.9 \times 10^{-6}$ for the PC run. Although both values are below the current constraint from *COBE*/FIRAS, $\langle y \rangle < 1.5 \times 10^{-5}$ (Fixsen et al. 1996), it is unlikely to be the case that the true background is as high as in the PC model, as this would erase many of the weak neutral hydrogen absorption lines seen towards quasars (Theuns, Mo & Schaye 2001; Shang, Crotts & Haiman 2007; Borgani & Viel 2009). The PC model therefore serves as an extreme test of the effect of a high background although we will remove the mean y signal in our analysis in Section 4.6 to mimic observations.

The contribution to the mean y signal from gas at different redshifts is shown in Fig. 3. The top panel shows results for all 50 maps in the GO simulation and the bottom panel for the PC simulation. Again, the difference between the two models is striking: the majority of the y signal comes from low redshift in the GO model (around 80 per cent from $z < 2$), whereas the opposite is true

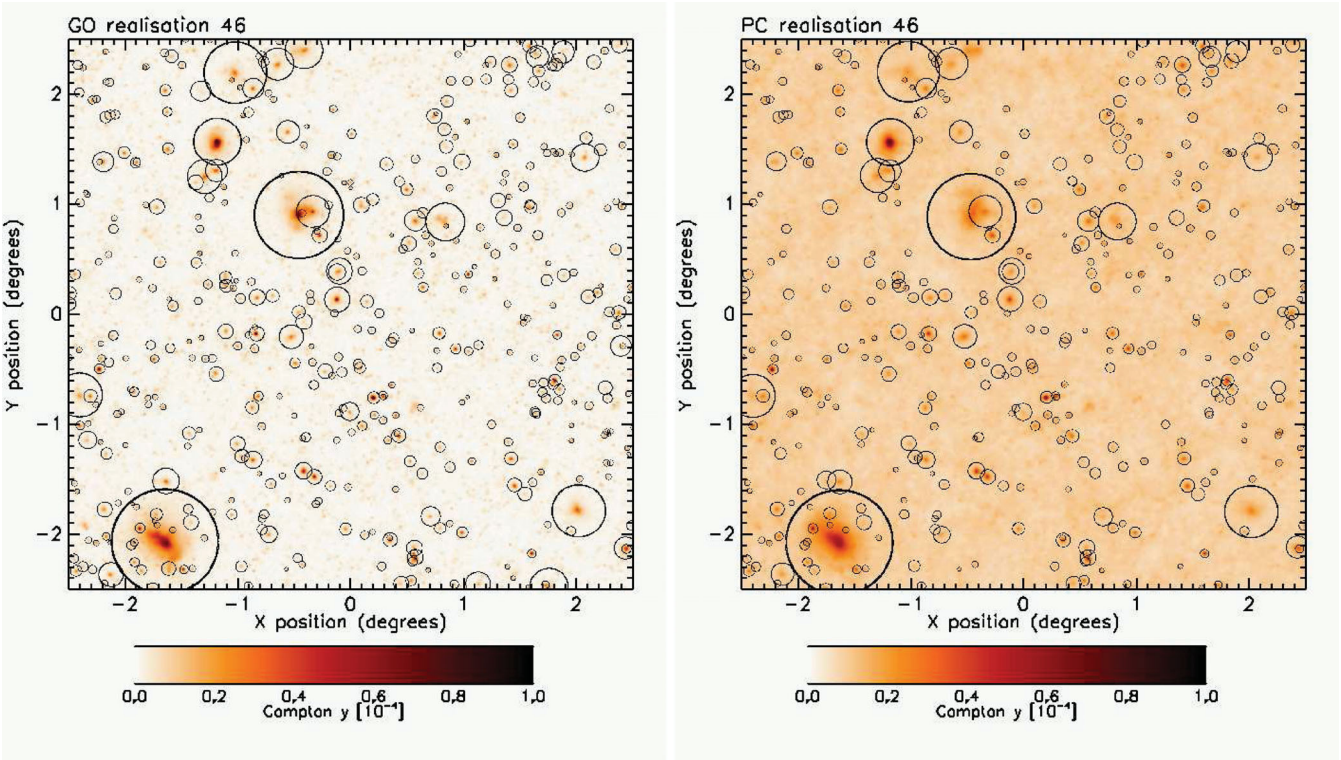

Figure 2. An example 5×5 deg^2 sky map of the Compton-y parameter from the GO (left-hand panel) and PC (right-hand panel) simulations. The maps were smoothed with a Gaussian kernel with a full width at half-maximum of 1 arcmin. Circles illustrating virial radii of all clusters with $M_{\rm vir} > 10^{14}\,h^{-1}\,{\rm M}_\odot$ are overlaid. Although both maps contain the same clusters, the PC map clearly has a larger background and the y distribution within each cluster is smoother, as seen in the maps of individual objects.

for the PC model (around 80 per cent from $z < 3.5$). Most of the mean y comes from overdense regions (groups and clusters) in the GO model that are more abundant at low redshift. In the PC case, most of the mean signal comes from mildly overdense gas at high redshift (da Silva et al. 2001). Note also that the contribution from gas at $z > 4$ is approximately zero in the PC model, unlike in the GO case, where there is a small but non-negligible signal. This difference is due to the inclusion of radiative cooling in the former model which removes most of the (small amount of) ionized gas at these redshifts.

3 HOT GAS PRESSURE PROFILES

Fundamental to understanding the SZ effect from clusters is the hot gas pressure profile, since we can write the SZ Y parameter for a spherically symmetric cluster as

$$Y_{500} = \frac{\sigma_{\rm T}}{m_{\rm e}c^2} \int_0^{r_{500}} P_{\rm e}(r)\, 4\pi r^3 {\rm d}\ln r, \qquad (13)$$

where $P_{\rm e} = n_{\rm e} k T_{\rm e}$ is the electron pressure. The contribution to Y_{500} will therefore be highest at the radius where $r^3 P_{500}$ is maximal. If the gas is in HSE, then the pressure profile ought to be structurally similar between different clusters since it is directly constrained by the underlying gravitational potential, which itself takes on a regular form (e.g. Navarro, Frenk & White 1997, hereafter NFW).

We construct and compare spherically averaged, hot gas mass-weighted pressure profiles using equation (11), for all clusters with $M_{500} > 10^{14}\,h^{-1}\,{\rm M}_\odot$ in our three (GO, PC and FO) models at $z = 1$ and 0. The profiles are rescaled such that we plot dimensionless quantities $x^3 P(x)/P_{500}$ against x, where $x = r/r_{500}$ and the scale pressure, $P_{500} \propto M_{500}^{2/3} E(z)^{8/3}$, is determined assuming a self-similar isothermal gas distribution (Voit 2005). If clusters formed a self-similar population, then these rescaled profiles would be identical for both varying mass and redshift.

Median scaled profiles are shown in Fig. 4, split into low-mass ($10^{14} < M_{500} \leq 5 \times 10^{14}\,h^{-1}\,{\rm M}_\odot$; triangles) and high-mass ($M_{500} > 5 \times 10^{14}\,h^{-1}\,{\rm M}_\odot$; squares) subsamples. Comparing the high-mass clusters between the three models at $z = 0$, it is immediately apparent that the largest contribution to Y_{500} comes from radii close to r_{500}, that is, where $P(r) \propto r^{-3}$. The profiles rise sharply (by around an order of magnitude) from the core outwards, then stay level or gradually decline at larger scales. The largest differences between the three models occur in the core region, where the PC and FO clusters have lower central pressures than the GO clusters due to the increase in core gas entropy from the extra heating.

The low-mass clusters have very similar median profiles to the high-mass clusters in the GO simulation, reflecting the similarity of objects in that model (Stanek et al. 2010). In the PC and FO models, however, the pressure profiles of the low-mass clusters have markedly different shapes from their high-mass counterparts. In particular, the scaled pressure in low-mass clusters is lower in the central region and is higher in the outer region, indicating that they are less concentrated than the high-mass clusters. Again this reflects the breaking of self-similarity caused by the feedback/preheating which has a larger effect in the lower mass clusters; the extra entropy given to the gas causes a redistribution to take place, pushing the gas out to larger radius.

Comparing the low-mass clusters at low and high redshift, the GO model shows little evolution (the core pressures are slightly lower), while clusters in the PC model have significantly lower core

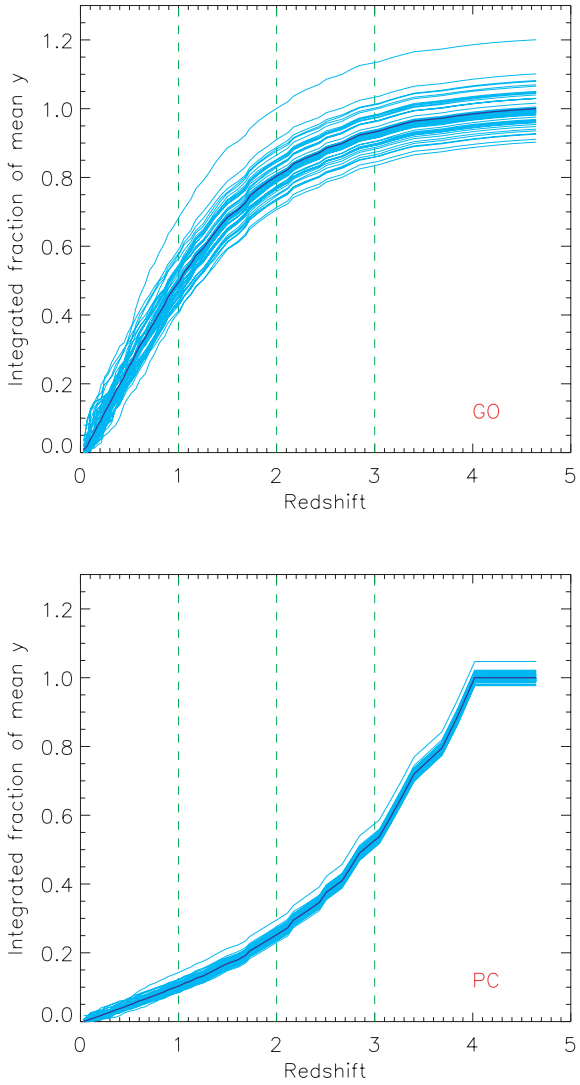

Figure 3. Integrated contribution to the overall mean y signal from gas below a given redshift. The top panel is for the GO simulation and the bottom panel for the PC simulation. Light curves are for individual maps and the dark curve is the average over all 50 maps. Each curve is normalized to the mean y averaged over all 50 maps, highlighting the scatter in the integrated signal between realizations. The simulations predict dramatically different redshift dependencies: the mean signal in the GO simulation comes from low redshfit ($z < 2$), whereas the opposite is the case for the PC simulation, due to the effect of preheating at $z = 4$.

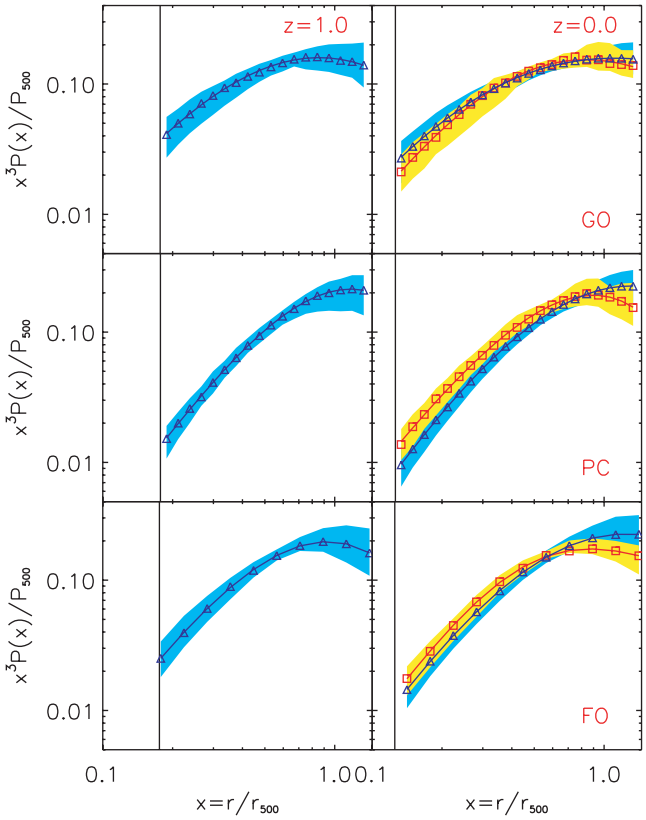

Figure 4. Scaled pressure profiles for clusters within the GO (top panels), PC (middle panels) and FO (bottom panels) simulations. The left-hand panels are $z = 1$ results and right-hand panels for $z = 0$. Median profiles are shown separately for low-mass ($10^{14} < M_{500} \leq 5 \times 10^{14}\, h^{-1}\, \mathrm{M}_{\odot}$; triangles) and high-mass ($M_{500} > 5 \times 10^{14}\, h^{-1}\, \mathrm{M}_{\odot}$; squares) clusters, respectively (note there are no high-mass clusters at $z = 1$). The yellow (cyan) shaded band illustrates the 16/84 percentiles (and thus represents the cluster-to-cluster scatter) for the high-mass (low-mass) subsample. The solid curves are best-fitting generalized NFW profiles to the median pressure profiles. The vertical solid line represents the radius where gravity is softened in the cluster with the smallest r_{500} (this is at a smaller radius than plotted for the FO model, for which a smaller softening was used, but we choose to use the same scale as in the other two models for ease of comparison). Note that the contribution to Y_{500} is predominantly from $r > 0.5r_{500}$ and so is not particularly susceptible to variations in the cluster core.

pressures at $z = 1$. This reflects the larger impact of the preheating on the gas at high redshift, since a cluster of fixed mass has a lower characteristic entropy at higher redshift from gravitational heating [$K \sim M^{2/3}E(z)^{-2/3}$]. Interestingly, the scaled pressure profiles in the FO model show little evolution with redshift, although the pressure in the outskirts ($r > r_{500}$) is higher at $z = 0$, reflecting the late-time heating of the gas by AGNs.

We also compare scaled pressure profiles between regular ($s \leq 0.1$) and disturbed ($s > 0.1$) clusters in Fig. 5, for our samples with $M_{500} > 10^{14}\, h^{-1}\, \mathrm{M}_{\odot}$. The largest differences between the two subsamples can be seen for the GO model, where the disturbed clusters (squares) have lower scaled pressure everywhere except around the maximum at $r \simeq 0.9r_{500}$. This is because the ongoing merger is compressing the gas (and therefore increasing its pressure) at large radius, while the inner region has yet to respond to the increase in the mass of the system. Note that since Y_{500} is proportional to the area under the pressure profile, there will be a noticeable offset in the Y_{500}–M_{500} relation, where a disturbed cluster has a smaller Y_{500} than a regular cluster with the same mass (see the next section). These differences are still present but at a lower level in the PC and FO models, where the higher entropy of the gas in lower mass clusters means that it is less easily compressed. This in turn leads to a negligible offset between regular and disturbed clusters in the Y_{500}–M_{500} relation, as we will show in the next section.

The shaded bands in Figs 4> and 5 illustrate the 16/84 percentiles for the two respective subsamples and thus give an indication of the cluster-to-cluster scatter. We show this more clearly in Fig. 6, where we have normalized the clusters in the low- and high-mass subsamples to the generalized NFW model that best fits the median profile (see below). Although the scatter at fixed radius is quite low compared with some other properties such as X-ray surface brightness, it is nevertheless appreciable and can be as high as 30–50 per cent beyond r_{500}. Thus, it is clearly not accurate to assume

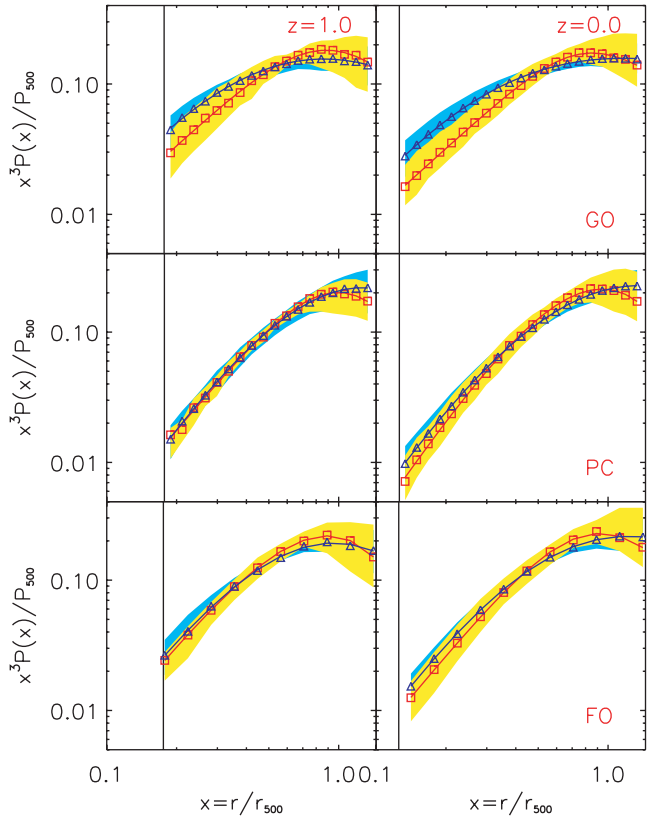

Figure 5. As in Fig. 4 but the samples are now split into regular ($s \leq 0.1$; triangles) and disturbed ($s > 0.1$; squares) subsamples. Disturbed (merging) clusters tend to have lower central pressures but higher peak values of $x^3P(x)$.

a single profile to describe all clusters, especially around r_{500} and beyond, where much of the SZ signal comes from.

3.1 Generalized NFW model

In a previous study of hot gas pressure profiles in cosmological simulations, Nagai et al. (2007b) found that the mean pressure profile of their simulated clusters could be well described by a generalized NFW (GNFW) model with five free parameters:

$$\frac{P(r)}{P_{500}} = \frac{P_0}{u^{\gamma}(1+u^{\alpha})^{(\beta-\gamma)/\alpha}}, \tag{14}$$

where $u = c_{500}x$, c_{500} is the concentration parameter, P_0 is the normalization parameter and (γ, α, β) determine the shape of the profile at small ($u \ll 1$), intermediate ($u \simeq 1$) and large ($u \gg 1$) radii, respectively. The GNFW model has been shown to provide a good description to the pressure profiles of X-ray groups and clusters (e.g. Arnaud et al. 2010; Sun et al. 2011) and is being used to optimize SZ cluster detection in data from the *Planck* satellite (e.g. Ade et al. 2011c, hereafter PXMM).

We have applied the GNFW model to our simulated clusters and the results for the median profiles can be seen as the solid curves in Figs 4 and 5. We also normalize our pressure profiles to the best-fitting median GNFW profile in Fig. 6. The residual values for our median profiles are also shown (as triangles and squares for our low- and high-mass subsamples) and are clearly at the per cent level. Such small residuals are not surprising, given the model contains five free parameters (once r_{500} is specified). The best-fitting parameter values themselves are listed in Table 2.

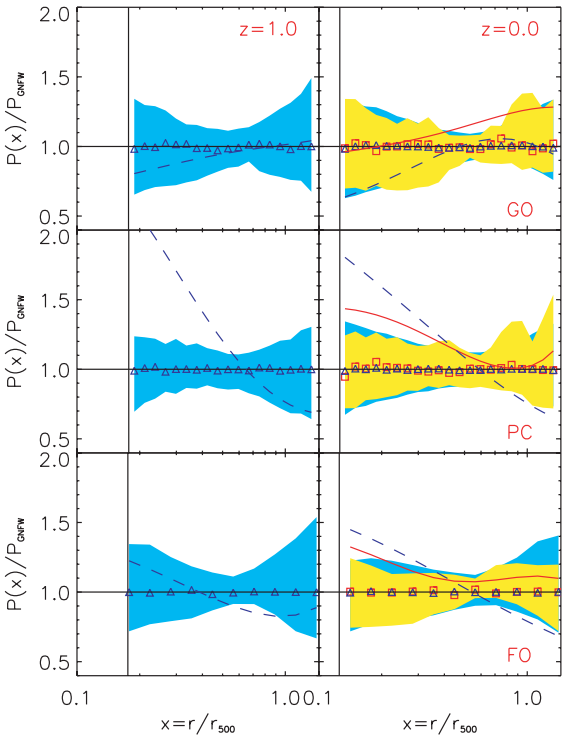

Figure 6. As in Fig. 4 but the median pressure profiles (and scatter) are now shown relative to their best-fitting generalized NFW model, clearly showing the size of cluster-to-cluster variations (that can be as large as 50 per cent). The solid and dashed curves are observed mean pressure profiles from low-redshift X-ray data (REXCESS; Arnaud et al. 2010), again scaled to our best-fitting generalized NFW model profiles, assuming the median mass from our low- and high-mass subsamples, respectively. In the outer regions ($r > 0.5r_{500}$), the high-mass clusters in the PC and FO models fit the latter profile quite well (to within 10 per cent or so), but the difference is larger for low-mass clusters, especially in the core regions.

Table 2. Best-fitting parameters for the generalized NFW model when applied to our median hot gas pressure profiles. Column 1 gives the redshift; column 2 the simulation model and cluster subsample (LM and HM refer to the low- and high-mass subsamples, respectively); and columns 3–7 the parameter values (see text for their meanings).

Redshift	Clusters	P_0	c_{500}	γ	α	β
$z = 0$	GO/LM	33.788	2.925	0.267	0.944	1.970
	PC/LM	6.317	0.517	0.090	0.901	1.603
	FO/LM	4.732	1.052	0.298	1.108	2.371
	GO/HM	6.756	1.816	0.519	1.300	2.870
	PC/HM	0.938	0.183	0.584	1.114	11.885
	FO/HM	3.210	1.974	0.605	2.041	2.989
$z = 1$	GO/LM	11.994	0.700	0.345	0.837	3.610
	PC/LM	0.856	0.539	0.512	1.447	4.038
	FO/LM	2.734	0.349	0.375	1.055	5.049

To investigate the distribution of GNFW parameters and any degeneracies that arise between parameters, we plot marginalized likelihood distributions for the FO model at $z = 0$ in Fig. 7. The full 5D likelihood distribution is estimated by fitting the GNFW model to individual clusters and computing the frequency of parameters $[\log_{10}P_0, \log_{10}c_{500}, \gamma, \alpha, \beta]$ over a 5D grid, which is then normalized such that the sum over all allowed parameter values is unity. We assume, as prior information, that the allowed range for each

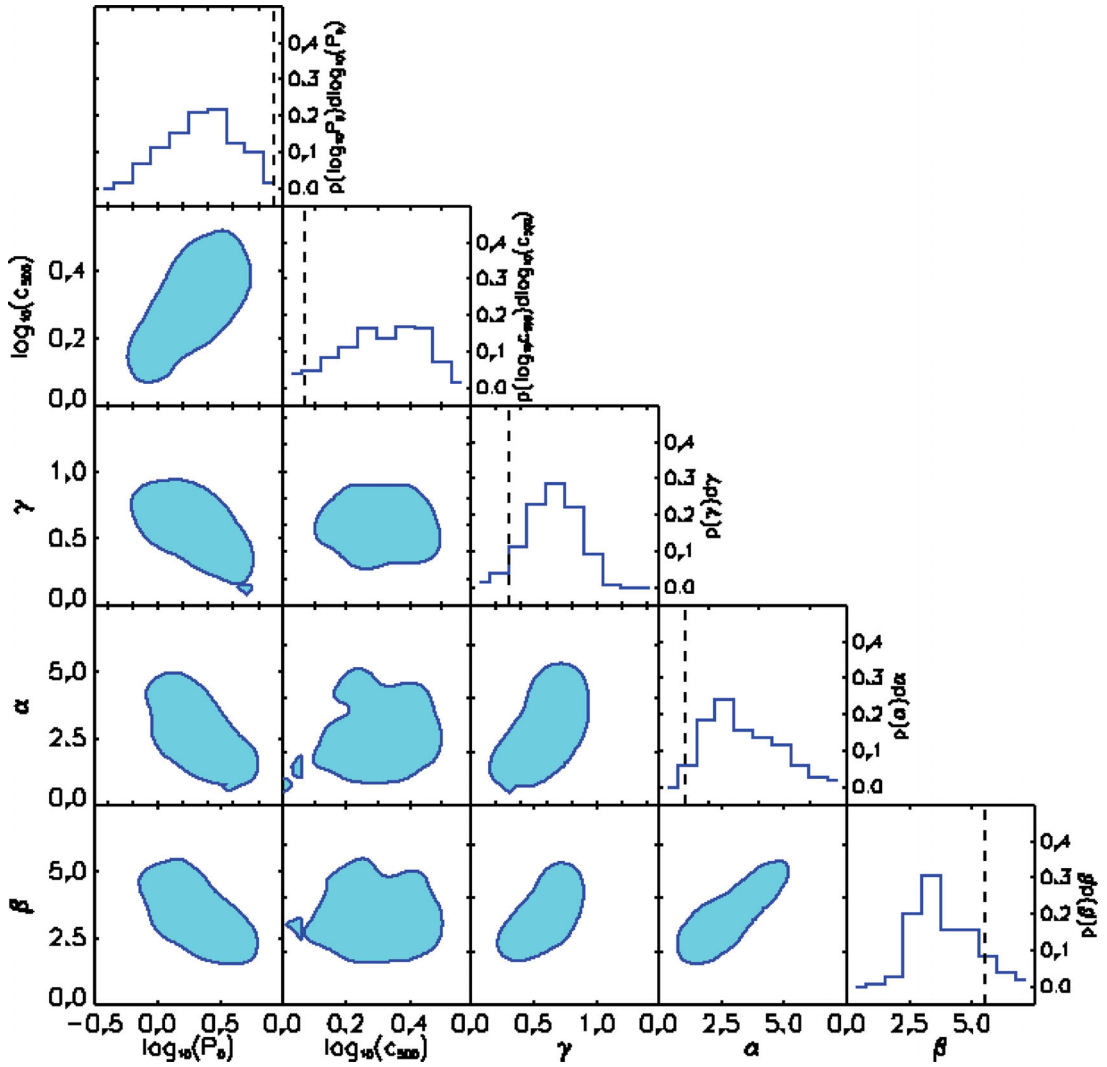

Figure 7. Estimated likelihood distributions for the best-fitting generalized NFW model parameters that describe the hot gas pressure profiles in the FO simulation at $z = 0$. The off-diagonal panels show 68 per cent confidence regions for the marginalized 2D distributions, for all parameter combinations. The diagonal panels show the 1D marginalized distributions for each parameter, with the best-fitting parameter values from REXCESS data overlaid as the dashed vertical lines. The three slope parameters (α, β, γ) are strongly correlated with one another and are all negatively correlated with the normalization, $\log_{10}P_0$. The concentration parameter, $\log_{10}c_{500}$, is only correlated with the normalization.

parameter is as specified on the axes in Fig. 7 and that each value is equally likely.

The diagonal panels in Fig. 7 show the marginalized 1D likelihood distributions for each of the five parameters, while the off-diagonal panels show the 68 per cent confidence regions for the full range of marginalized 2D distributions, smoothed to reduce noise. The concentration parameter is strongly correlated with the normalization parameter but does not correlate strongly to any of the slope parameters. Interestingly, the normalization is anticorrelated (and therefore degenerate) with the slope parameters. Finally, the slope parameters are strongly correlated with one another. It is therefore clear that a simpler model with fewer slope parameters could potentially be found that describe these simulated data. However, the flexibility of the GNFW model allows a wide range of profiles to be accurately described using a simple formula. This is especially true when cool-core clusters are included; these are absent in our current models and so we plan to extend our work to investigate cooling effects in a future study.

3.2 Comparison with observational data

We also compare the simulated profiles with the pressure profile presented by Arnaud et al. (2010), compiled from low-redshift X-ray observations (for $r < r_{500}$; the REXCESS sample) and other numerical simulations (for $r > r_{500}$). It therefore provides information on the realism of our simulated pressure profiles as well, providing a useful comparison with other simulations (on large scales).

The Arnaud et al. (2010) profile is based on the GNFW model modified to account for additional (weak) mass dependence in the observational data:

$$P(x) = P_{\rm GNFW}\left(\frac{M_{500}}{3\times10^{14}\,{\rm M}_{\odot}}\right)^{\alpha_{\rm P}}, \qquad (15)$$

where $P_{\rm GNFW}$ is the GNFW pressure profile given in equation (14) with parameters, $[P_0, c_{500}, \gamma, \alpha, \beta] = [8.403, 1.177, 0.3081, 1.0510, 5.4905]$ and $\alpha_{\rm P} = 0.12$. We show this profile, evaluated for the median mass values of our two subsamples, in Fig. 6; the dashed curve is for the low-mass sample, plotted relative to our best-fitting GNFW profile, while the solid curve is for the high-mass sample.

The Arnaud et al. parameters are also shown as the dashed lines in Fig. 7.

Comparing with our $z = 0$ results, as is most appropriate, the median GO profiles agree to within 30 per cent or so, over the plotted range of radii and for both mass ranges. For the PC and FO clusters, the agreement is very good at large radius ($>0.5r_{500}$) for high-mass clusters, where the Arnaud et al. profile is only around 10 per cent higher and within the intrinsic scatter of our simulated profiles. The low-mass clusters are more discrepant, with the steeper Arnaud et al. profile being 20–30 per cent lower at r_{500}. This suggests that our simulated clusters contain gas that is at higher pressure at r_{500} than in those used for the Arnaud et al. profile at large radius. Given that the feedback in our models is likely to be stronger than in the simulations used in the Arnaud et al. study, this discrepancy in pressure is probably due to the effects of radiative cooling, absent in our models and likely significant in the other simulations (see the discussion in Section 4.4; we also note that Arnaud et al. already corrected for the effects of baryon fraction). Even larger differences are present in the inner regions; there, the Arnaud et al. profile is significantly higher than our simulated results. Again, cooling is the likely culprit here as its effect is strongest in the densest regions.

An important uncertainty in the observed profile estimation is the effect of hydrostatic bias, that is, systematic offsets in r_{500} and M_{500} from their true values, when estimated from the equation of HSE. As we will show in Section 5, hydrostatic mass is biased low with respect to the true mass and is most significant for the GO model (the estimated-to-true mass ratio is around 0.7 for the GO model, compared to around 0.9 for the PC/FO models). The effect of this bias is to increase the scaled pressure at fixed scaled radius, as both the scale radius, r_{500}, and the scale pressure, $P_{500} \propto M_{500}^{2/3}$, decrease, on average. We discuss the effect of hydrostatic bias on the Y_{500}–M_{500} relation in detail in Section 5 but note here that we have explicitly checked how this affects the pressure profiles for each model. To do this, we first redefined our subsamples using the estimated masses. We then compared the shift in pressure at the estimated value of r_{500} between the median scale profile and the Arnaud et al. profile, for both low-mass and high-mass subsamples. We also recomputed the pressure profiles using the spectroscopic-like temperature, rather than the hot gas mass-weighted temperature, as this will be closer to the X-ray temperature profile used by Arnaud et al.

We find that the combined effect of these changes is largest for the GO model, where the median pressure profiles from both subsamples are now within 10 per cent of the Arnaud et al. values at r_{500}. The increase in the scaled pressure profile due to hydrostatic bias is counteracted by a decrease due to the use of spectroscopic-like temperature, which is lower than the mass-weighted temperature for this model (see Section 4.2). The two effects are smaller for the PC and FO models and so we see very similar results to those before these changes were applied. Thus, the scaled pressure profiles for the low-mass clusters in these models are still around 30 per cent lower than the Arnaud et al. profile at r_{500}.

4 SZ SCALING RELATIONS

We now present SZ scaling relations for our simulations and compare them specifically with the recent analysis of data from *Planck* and *XMM–Newton*. We will also compare our results with recent simulations before going on to consider the effect of projection of large-scale structure along the line of sight. The effect of hydrostatic bias on the scaling relations will be considered in the next section.

We consider the scaling relations between Y_{500} and several other properties: the total mass, M_{500}; the hot gas mass, $M_{\rm gas,500}$; the X-ray spectroscopic-like temperature, $T_{\rm sl}$; and the analogous X-ray quantity to Y_{500}, $Y_{\rm X,500}$. We note that the $Y_{\rm X}$–M_{500} relation (not considered here) has already been presented by Short et al. (2010) and scaling relations for the lower density contrast, $\Delta = 200$, for the GO and PC models by Stanek et al. (2009).[4]

We follow the standard procedure and assume that the mean relationship between Y_{500} and the independent variable can be adequately described by a power law and is thus a linear relationship in log-space.[5] We estimate the slope and normalization of the relation by performing a least-squares fit to the data

$$E(z)^{\gamma} Y_{500} = 10^{A} \, (X/X_0)^{B} \, , \tag{16}$$

where A and B describe the best-fitting normalization and slope, respectively, and X_0 is the pivot point, suitably chosen to minimize covariance between the two parameters. For the power-law index γ we choose the appropriate value for self-similar evolution, so if our clusters evolve self-similarly we should see no change in the best-fitting parameters A and B.

We also estimate the scatter in $\log_{10}(Y_{500})$, $\sigma_{\log_{10} Y}$, as

$$\sigma_{\log_{10} Y} = \sqrt{\frac{1}{N-2} \sum_{i=1}^{N} \left[\log_{10} Y_i - \log_{10} Y_{\rm bf}(X_i)\right]^2}, \tag{17}$$

where the index i runs over all N clusters included in the fit and $Y_{\rm bf}$ is the best-fitting Y_{500} value for a cluster with property, X_i. Note that the scatter in $\ln Y$ is simply $\sigma_{\ln Y} = \ln(10)\, \sigma_{\log_{10} Y}$.

4.1 The Y_{500}–M_{500} relation

The most important scaling relation is that between SZ flux and mass. We present our Y_{500}–M_{500} relations in Fig. 8 for the GO model (top panels), PC model (middle panels) and FO model (bottom panels). Results are shown both for $z = 1$ (left-hand panels) and $z = 0$ (right-hand panels). The best-fitting relation to all clusters in each panel with $10^{14} < M_{500} < 10^{15}\, h^{-1}\, {\rm M}_{\odot}$ is shown as a solid line (best-fitting parameter values and their uncertainties are listed in Table 3).

It is clear that there is a very tight correlation between Y_{500} and M_{500} in all three models at both low and high redshift. At $z = 0$ the intrinsic scatter about the best-fitting power-law relation is only $\sim$4 per cent, with sub-per cent variations between models, making this particular relation one of the tightest known cluster scaling relations involving gas; this finding is consistent with previous simulations with fewer clusters (e.g. da Silva et al. 2004; Nagai 2006). The distribution of residual Y_{500} values about the best-fitting relation is well described by a lognormal distribution of width $\sigma = \sigma_{\ln Y}$ (Fig. 9). This is in agreement with previous work (e.g. Stanek et al. 2010; Fabjan et al. 2011).

The normalization of the $z = 0$ relation also varies very little between models, the maximum variation being around 7 per cent. The best-fitting slope also varies by around 7 per cent, from 1.67 in the FO model (very close to the self-similar value of 5/3) to 1.79 in

[4] We have independently verified that our GO and PC results, when using $\Delta = 200$, are consistent with theirs, but as was pointed out by Viana et al. (2011) the Y_{200} values given in Stanek et al. (2009) quoted with incorrect units.

[5] Stanek et al. (2010) present quadratic fits to the PC data but we find this only to be important when the lower mass groups are included, as was the case in that study.

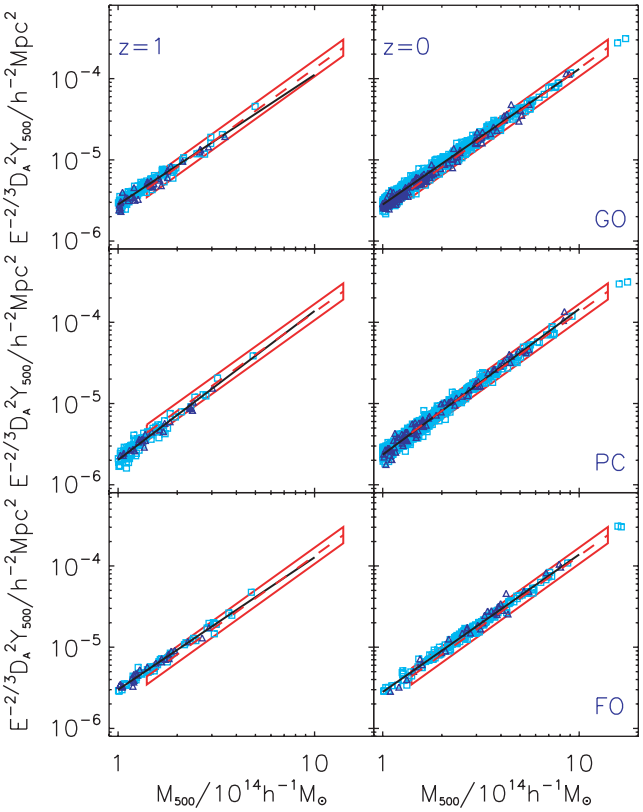

Figure 8. Scaling relations between the SZ flux, Y_{500}, and total mass, M_{500}, for the GO (top panels), PC (middle panels) and FO (bottom panels) models at $z = 1$ (left-hand panels) and $z = 0$ (right-hand panels). The Y_{500} values at $z = 1$ are rescaled such that no change in the relation corresponds to self-similar evolution [$Y_{500} \propto E(z)^{2/3}$ at fixed mass]. The solid diagonal line is a least-squares fit to the relation. The best-fitting power law to $z < 0.5$ *Planck*/*XMM–Newton* data (PXMM) is shown in all panels as a dashed line, while the box illustrates the intrinsic scatter in the observed relation. The triangles represent disturbed clusters (with $s > 0.1$), while the squares are regular clusters. The results are very similar for all three models and there is no evidence for significant departure from self-similar evolution.

the PC model. As discussed in Short & Thomas (2009) for the Y_X–M_{500} relation, the similarity between the models can be explained by the increase in gas temperature compensating for the drop in gas mass, required to maintain virial equilibrium (since $Y \propto M_{gas}T$ and is thus proportional to the total thermal energy of the gas). The agreement between the GO and PC/FO models is better here than for the Y_X–M_{500} relation as Y_X is defined using the spectroscopic-like temperature, T_{sl}, which is weighted more heavily by low-entropy gas; we discuss this point further below.

We have also investigated the dependence of the Y_{500}–M_{500} relation on redshift. In the left-hand panels of Fig. 8, we present results for $z = 1$, allowing a simple comparison to be made with the $z = 0$ results for each model. It is evident that the clusters evolve close to the self-similar expectation in all three models, given that the normalization and slope change very little between the two redshifts (see also Table 3). To quantify this further, we have also plotted the best-fitting normalization, slope and scatter as a function of redshift in Fig. 10, where we used all available outputs from $z = 0$ to 1. (Equivalent plots for the other scaling relations are provided in the appendix.)

The dependence of the best-fitting slope on redshift for all three models is shown in the top panels of Fig. 10. For clarity, we normalize the slope to the median value at $z < 0.3$ and the yellow bands indicate the uncertainties (using the 16/84 percentile values). All three models are consistent with no evolution in slope to $z = 0.3$, then some mild evolution is seen at higher redshift, where the number of massive clusters drops. This evolution is very minor, however, as the slope remains within around 5 per cent of the low-redshift value.

The variation in normalization with redshift is shown in the middle panels of Fig. 10. Here, we have fixed the slope at the $z < 0.3$ median value and just allowed the single normalization parameter to vary. Again, we factored out the self-similar evolution and normalized to the $z = 0$ result, so a value consistent with zero corresponds to self-similar evolution. In the GO and PC cases, the normalization is consistent with self-similar evolution to $z = 0.3$; afterwards, there is some negative evolution (i.e. the relation evolves slightly more slowly than predicted from the self-similar model), especially in the PC case. The FO model shows different behaviour: at low redshift ($z < 0.3$), Y_{500} increases more rapidly with redshift than the self-similar case (at fixed mass), then at higher redshifts evolves in accordance with the self-similar expectation. These differences in evolution are likely to be real and reflect the varying gas physics. In the GO case, the gas at high redshift is slightly colder than expected (due to an increase in the merger/accretion rate leading to a larger residual unthermalized component). In the PC case, the high-redshift preheating leads to a deficit in gas mass but the clusters start to recover at low redshift as the entropy scale at fixed mass set by gravitation is larger. Finally, in the FO case, the feedback from black holes is stronger at late times, leading to a decrease in gas content (Short et al. 2010). In all three cases, however, the effect on the normalization is still small; the largest change is from the PC model at $z = 1$ where only a 10 per cent decrease is seen.

Finally, we illustrate how the scatter in the Y_{500}–M_{500} relation evolves with redshift in the bottom panels of Fig. 10. The $z = 0$ value is also shown as a dashed horizontal line for clarity. Again, the picture is consistent with minimal change; the scatter only increases to $z = 1$ by 0.01 or so in the GO and PC cases, and decreases by less than 0.01 in the FO case.

4.2 Relationship between Y_{500} and observables

We also present scaling relations between Y_{500} and other key X-ray observables. Fig. 11 shows Y_{500}–$M_{gas,500}$ relations, laid out as before. This relation is interesting to study because it essentially probes non-self-similar behaviour in the mass-weighted temperature, T_m, of the gas, since $Y \propto M_{gas}T_m$ and thus M_{gas} appears on both axes. Here we fit data within the range, $2 \times 10^{13} < M_{gas,500} < 2 \times 10^{14}\,h^{-1}\,M_\odot$. As with the Y_{500}–M_{500} relation, the slope from the GO model at $z = 0$ is close to the self-similar value of 5/3. The PC and FO models have shallower slopes, due to the increase in the temperature of the gas in low-mass clusters. As might be expected, the scatter in the relation is even tighter than for the Y_{500}–M_{500} relation, and is typically 0.02–0.03. The distribution of the scatter is also close to lognormal. From comparing the $z = 1$ and $z = 0$ results, both the GO and PC models predict evolution that is close to self-similar (the normalization is within 5 per cent of the $z = 0$ value out to $z = 1$), but the FO relation evolves more slowly with redshift (~10 per cent lower at $z = 1$), again due to the increase in feedback from the AGN at late times which additionally heats the gas. This evolutionary behaviour is confirmed when studying the relation at all available redshifts from $z = 0$ to 1, in Fig. A1, which also shows that the slope and scatter vary little.

Table 3. Best-fitting parameters for simulated SZ scaling relations at $z = 0$ and 1. Column 1 gives the scaling relation being considered; column 2 the pivot point (in appropriate units); column 3 the redshift; column 4 the simulation model; and columns 5, 6 and 7 give the best-fitting values for the normalization, power-law index and scatter in $\log_{10} Y_{500}$, respectively. Quoted uncertainties correspond to either the 16th or 84th percentile (whichever is largest), estimated using the bootstrap resampling technique.

Relation	X_0	Redshift	Model	A	B	$\sigma_{\log_{10} Y}$
$E(z)^{-2/3}Y_{500}$–M_{500}	$3 \times 10^{14}\,h^{-1}\,\mathrm{M}_\odot$	$z = 0$	GO	-4.754 ± 0.002	1.670 ± 0.007	0.041 ± 0.001
			PC	-4.774 ± 0.003	1.794 ± 0.009	0.045 ± 0.001
			FO	-4.744 ± 0.003	1.69 ± 0.02	0.043 ± 0.003
		$z = 1$	GO	-4.79 ± 0.01	1.60 ± 0.04	0.048 ± 0.003
			PC	-4.82 ± 0.01	1.83 ± 0.04	0.059 ± 0.005
			FO	-4.75 ± 0.01	1.63 ± 0.04	0.037 ± 0.004
$E(z)^{-2/3}Y_{500}$–$M_{\mathrm{gas},500}$	$3 \times 10^{13}\,h^{-1}\,\mathrm{M}_\odot$	$z = 0$	GO	-5.098 ± 0.001	1.650 ± 0.007	0.029 ± 0.001
			PC	-4.887 ± 0.001	1.478 ± 0.008	0.018 ± 0.001
			FO	-4.889 ± 0.003	1.45 ± 0.01	0.025 ± 0.002
		$z = 1$	GO	-5.145 ± 0.004	1.61 ± 0.03	0.034 ± 0.003
			PC	-4.844 ± 0.006	1.46 ± 0.05	0.016 ± 0.005
			FO	-5.007 ± 0.004	1.53 ± 0.03	0.028 ± 0.006
$E(z)Y_{500}$–T_{sl}	5 keV	$z = 0$	GO	-4.27 ± 0.03	2.5 ± 0.2	0.19 ± 0.02
			PC	-4.706 ± 0.006	3.16 ± 0.04	0.060 ± 0.002
			FO	-4.665 ± 0.006	3.11 ± 0.07	0.078 ± 0.007
		$z = 1$	GO	-4.03 ± 0.07	3.0 ± 0.6	0.16 ± 0.07
			PC	-4.910 ± 0.006	3.38 ± 0.06	0.047 ± 0.004
			FO	-4.54 ± 0.02	2.8 ± 0.1	0.086 ± 0.009
$E(z)^{-2/3}Y_{500}$–$E(z)^{-2/3}Y_{\mathrm{X},500}$	$1 \times 10^{-5}\,h^{-2}\,\mathrm{Mpc}^2$	$z = 0$	GO	-4.952 ± 0.003	1.049 ± 0.008	0.058 ± 0.002
			PC	-5.020 ± 0.001	1.002 ± 0.002	0.015 ± 0.001
			FO	-5.012 ± 0.001	0.998 ± 0.004	0.018 ± 0.001
		$z = 1$	GO	-4.882 ± 0.009	1.05 ± 0.03	0.052 ± 0.004
			PC	-5.015 ± 0.002	0.999 ± 0.004	0.009 ± 0.001
			FO	-5.007 ± 0.003	0.99 ± 0.01	0.020 ± 0.004

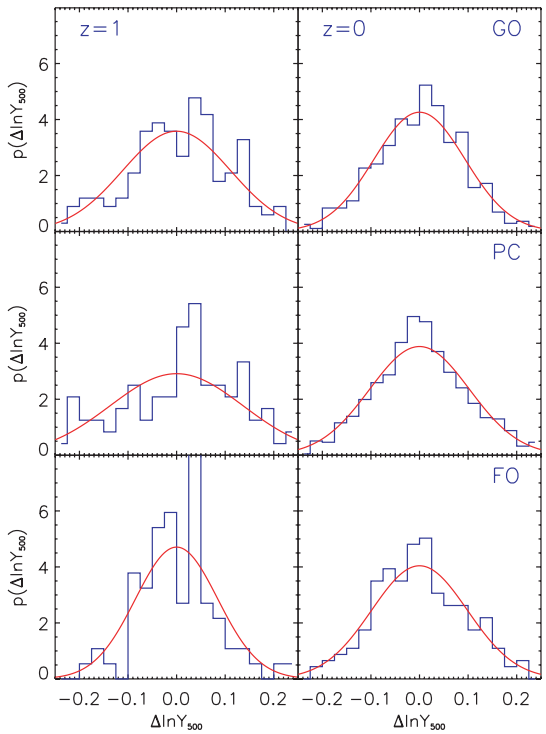

Figure 9. Distribution of residual Y_{500} values about the best-fitting Y_{500}–M_{500} relation, plotted using natural logarithms, for each of the models at $z = 1$ and 0. A normal distribution of width $\sigma = \sigma_{\ln Y}$ is overlaid; it is clear that this provides a good description of the scatter.

We also consider scaling relations between Y_{500} and X-ray spectroscopic-like temperature, T_{sl}, and show results in Fig. 12, with the redshift dependence of the slope, normalization and scatter illustrated in Fig. A2. Here, we further restrict our sample to contain only clusters with $kT_{\mathrm{sl}} > 3$ keV, as the spectroscopic-like temperature only applies to hot clusters where thermal bremsstrahlung dominates the X-ray emission. This reduces our samples to 136 (12), 583 (102) and 179 (73) clusters at $z = 0$ ($z = 1$) in the GO, PC and FO models, respectively. Note the more severe reduction in the GO case; the non-gravitational heating in the PC and FO models increases T_{sl} at fixed mass, relative to the GO case, and thus increases the number of clusters in their X-ray temperature-limited samples. Best-fitting relations are then calculated for clusters in the range, $3 < kT_{\mathrm{sl}} < 10$ keV.

The GO model relation has a slope which is consistent with the self-similar expectation ($B = 5/2$) at $z = 0$ and 1. The relation evolves slightly faster than the self-similar model (the normalization is around 10 per cent higher than expected at $z = 1$), while the scatter is approximately constant at all redshifts, but is much higher than for the previous relations ($\sigma_{\log_{10} Y} \simeq 0.15$–$0.2$). This last point is due to T_{sl} being a much noisier property as it is sensitive to the clumpy, low entropy gas that is prevalent in this model. We also note that the scatter is poorly described by a lognormal distribution. In comparison, the PC and FO models, which have much smoother gas, typically have lower scatter, $\sigma_{\log_{10} Y} \simeq 0.05$–$0.1$, which is well described by a lognormal distribution. The slope in these two models is significantly steeper ($B \simeq 3$) and the evolution of this relation shows the largest departure from self-similarity (up to 20 per cent lower/higher at $z = 1$ in the PC/FO model).

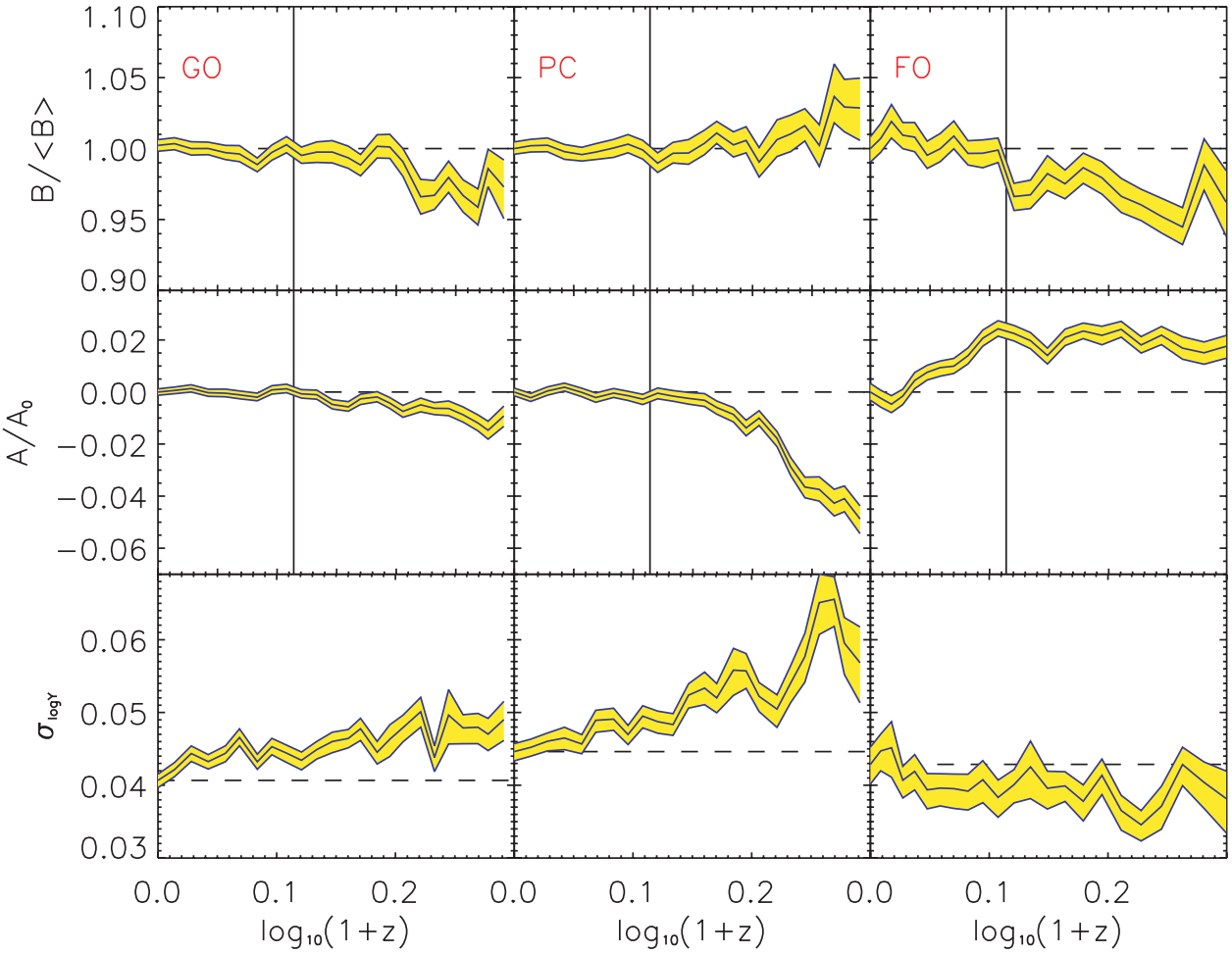

Figure 10. The dependence of the slope, normalization and scatter of the $E(z)^{-2/3}Y_{500}$–M_{500} relation with redshift, for the GO (left-hand panels), PC (middle panels) and FO (right-hand panels) simulations. Results are plotted from $z = 0$ to 1. In the top panels, the best-fitting slope at each redshift is normalized to the median slope for outputs at $z < 0.3$ (shown as a vertical line). The middle panels illustrate the redshift dependence of the normalization after the self-similar dependence has been taken out; the normalization is divided by the $z = 0$ value in this case. In the bottom panels, the rms scatter in $\log_{10}Y$, $\sigma_{\log_{10}Y}$, is shown as a function of redshift. For both the normalization and scatter values, the slope was fixed to the $z < 0.3$ median value when performing the fits. The bands in all panels illustrate 16 and 84 percentiles, calculated by bootstrap resampling the data. All three models predict very little evolution in the slope and normalization of the $E(z)^{-2/3}Y_{500}$–M_{500} relation to $z = 1$ and the intrinsic scatter remains small ($\sigma_{\log_{10}Y} < 0.06$).

Finally, in Fig. 13 we plot Y_{500} against $Y_{\rm X,500}$ for our cluster samples and show the redshift dependence of the scaling relation parameters in Fig. A3. We do this to directly highlight how the choice of gas temperature affects the results: any deviation from $Y_{500} = Y_{\rm X,500}$ must be due to differences between mass- and X-ray-weighted temperatures. No significant deviation is seen in the PC and FO models (the difference in normalizations at $E(z)^{-2/3}Y_{\rm X,500} = 10^{-5}\,h^{-2}\,{\rm Mpc}^2$ is less than 5 per cent) and there is very little scatter ($\sigma_{\log_{10}Y} \simeq 0.01$–$0.02$) at low and high redshift, which again has a distribution that is lognormal. The GO model, on the other hand, shows a significant bias, such that $Y_{500} \simeq 1.1Y_{\rm X,500}$ at $z = 0$, increasing to $Y_{500} \simeq 1.3Y_{\rm X,500}$ at $z = 1$. The scatter is also significantly larger than for the other two models, $\sigma_{\log_{10}Y} \simeq 0.05$, and the distribution is skewed to lower values. Again, these results demonstrate that the clumpier gas in the GO model has a stronger effect on the X-ray properties than on the SZ properties. As we shall see in Section 5, this has important consequences for our hydrostatic mass estimates.

4.3 Effect of dynamical state

It is also interesting to consider whether clusters undergoing mergers are offset from the main Y_{500} scaling relations as they could add to the intrinsic scatter. We mark our *disturbed* ($s > 0.1$) subsamples as triangles in each of the figures presenting scaling relations, discussed above (Figs 8–13). Note that while a large value of s is indicative of an ongoing merger, not all dynamically disturbed clusters have large values of s (Rowley, Thomas & Kay 2004).

As predicted from studying the hot gas pressure profiles in Section 3, the only significant offset seen between regular and disturbed clusters is for the GO model, where disturbed objects lie slightly below the Y_{500}–M_{500} and Y_{500}–$M_{\rm gas,500}$ relations, and above the Y_{500}–$Y_{\rm X,500}$ relation (there are not enough disturbed clusters to say anything conclusive for the Y_{500}–$T_{\rm sl}$ relation). This suggests that there is a significant difference in the fraction of unthermalized energy between regular and disturbed clusters in this model. In the case of the Y_{500}–M_{500} and Y_{500}–$M_{\rm gas,500}$ relations, the

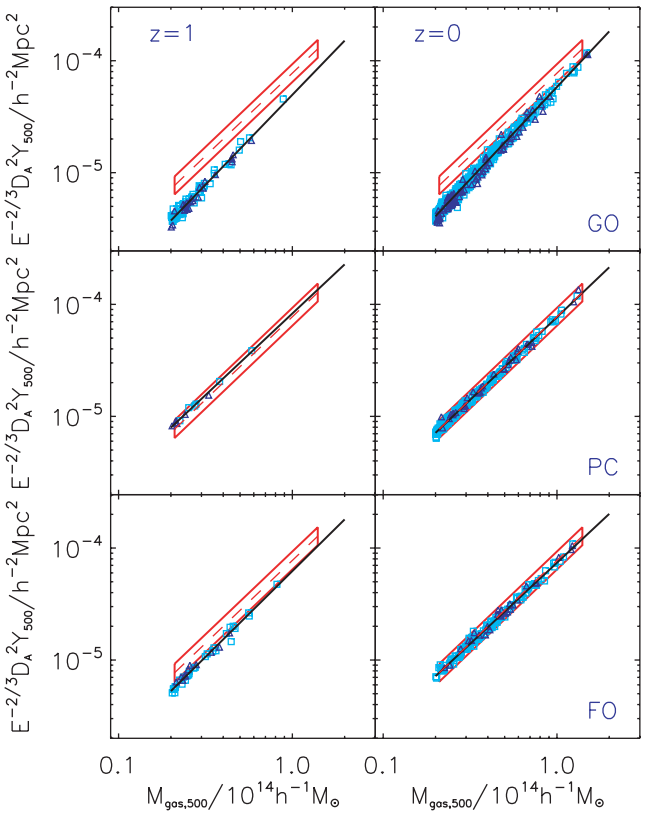

Figure 11. Scaling relations between Y_{500} and hot gas mass, $M_{\rm gas,500}$ for the GO, PC and FO models at $z = 1$ and 0. Details for each panel are the same as described in Fig. 8. The scatter is particularly small for the simulated version of this relation as the quantities plotted on the two axes are strongly correlated.

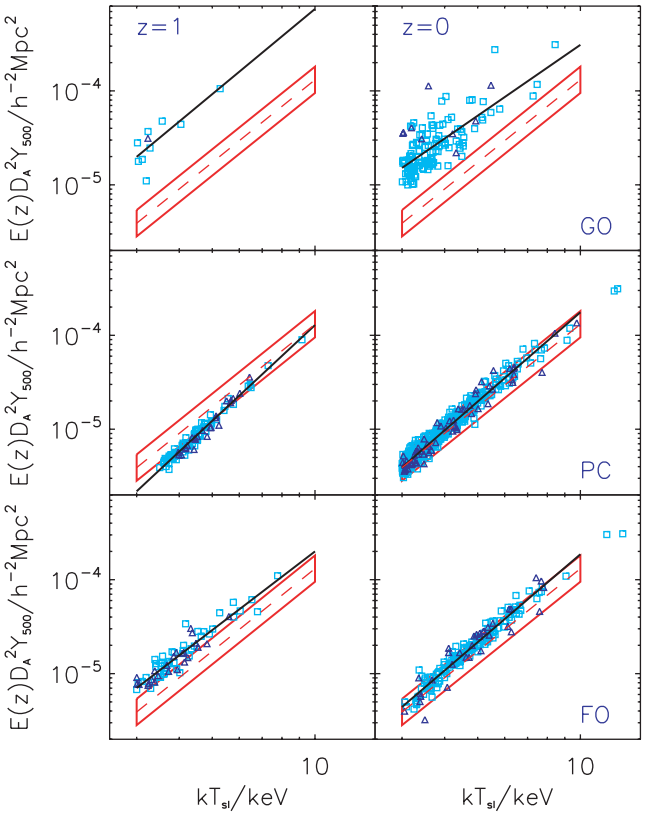

Figure 12. Scaling relations between Y_{500} and X-ray spectroscopic-like temperature, $T_{\rm sl}$, evaluated outside the core. Details for each panel are the same as described in Fig. 8. This relation has relatively large scatter for both the observations and simulations, since $T_{\rm sl}$ is a noisier property than the other observables being considered in this study.

mass-weighted temperature is lower for disturbed clusters of the same mass than regular clusters, leading to the negative offset. The effect is exacerbated when $T_{\rm sl}$ is considered (since it is weighted towards the cooler component), leading to a positive offset in the Y_{500}–$Y_{\rm X,500}$ relation.

4.4 Comparison between Y_{500}–M_{500} relations from other simulations

Given the importance of the Y_{500}–M_{500} relation for cosmological applications and its apparent insensitivity to cluster gas physics, it is important to compare our results to those from other groups using different simulations. A number of studies have been performed with varying assumptions for both the cosmology and the gas physics, as well as the use of different algorithms for the N-body and hydrodynamics solvers (e.g. White et al. 2002; da Silva et al. 2004; Motl et al. 2005; Nagai 2006; Bonaldi et al. 2007; Hallman et al. 2007; Aghanim et al. 2009; Yang et al. 2010; Battaglia et al. 2011; Krause et al. 2012).

We choose to compare our results with the work of Nagai (2006) and Krause et al. (2012) for two reasons. First, both groups presented results for $\Delta = 500$ and are thus most readily comparable with ours. Secondly, the two groups used very different codes, so it is useful to also include that uncertainty in our comparison. In Fig. 14 we compare our best-fitting Y_{500}–M_{500} relation at $z = 0$ from the FO model (solid line) with the results of these authors. To highlight the differences between simulations, we normalize all results to our best-fitting FO relation. We also have to make a correction for the different baryon fractions used in the simulations, since $Y \propto f_{\rm b}$. In both cases, the baryon fraction is lower than our adopted value of $f_{\rm b} = 0.18$ (Nagai 2006 assumed $f_{\rm b} = 0.14$ and Krause et al. 2012 assumed $f_{\rm b} = 0.133$). Note that this is not a perfect correction as it does not account for the non-self-similar behaviour of the baryon fraction with cluster mass.

Nagai (2006) presented results for 11 clusters simulated with the ART code (e.g. Kravtsov, Klypin & Hoffman 2002), which uses the adaptive mesh refinement technique to model hydrodynamics. Two sets of runs were studied, a non-radiative run (labelled AD) and a run with cooling and star formation (labelled CSF). Out of the 11 clusters, six have $M_{500} > 10^{14}\,h^{-1}\,{\rm M}_\odot$ (cf. our FO model with 188 clusters in this mass range). The upper dot–dashed line in Fig. 14 is their best-fitting relation to the AD clusters. The slope of their relation (1.66 ± 0.09) is in agreement with our (non-radiative) GO result (1.670 ± 0.007; dashed line), while the normalization is within 10 per cent of ours. Such good agreement is reassuring, given the different hydrodynamic methods used, although the large difference in sample size must be borne in mind. Their CSF result is shown as the lower dot–dashed curve in Fig. 14; comparing with our FO relation, their normalization is significantly lower (20–30 per cent). As the author points out, the reduction in SZ signal in the CSF run is mainly due to the lower gas fraction caused by (over)cooling and star formation which removes hot gas from the ICM. As we discussed earlier, the gas fractions in the FO run are also lower than in the non-radiative case but the mechanism responsible

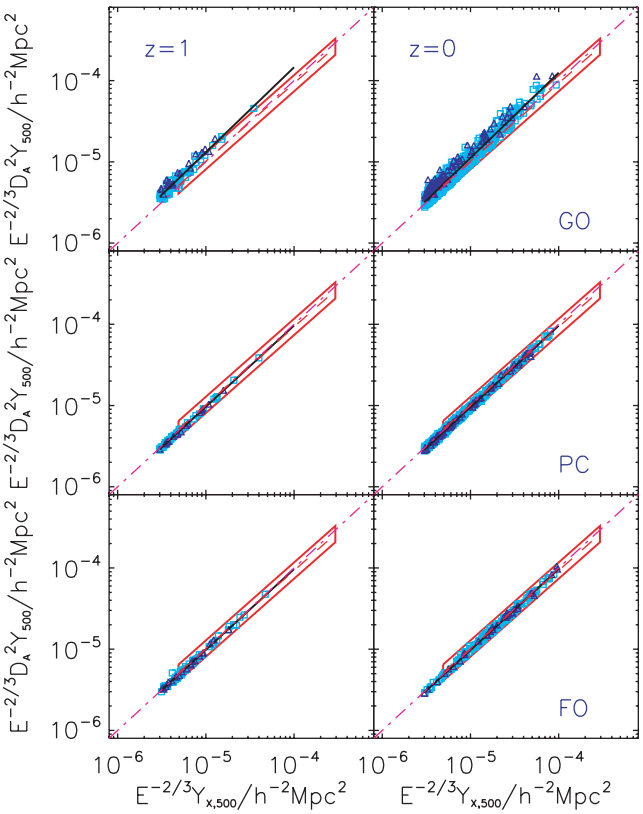

Figure 13. Scaling relations between the SZ Y_{500} and X-ray analogue, $Y_{X,500}$. Details for each panel are the same as described in Fig. 8. The dot–dashed line corresponds to $Y_{500} = Y_{X,500}$; only the GO simulation shows a significant offset from this relation, due to the presence of clumpy low-entropy gas.

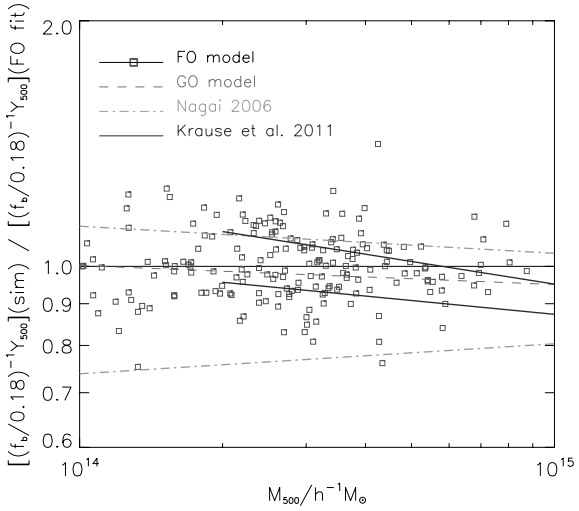

Figure 14. Comparison between the FO Y_{500}–M_{500} scaling relation and results from other simulations at $z = 0$. All results are normalized to the best-fitting FO Y_{500}–M_{500} relation, and Y_{500} values from other simulations have been rescaled to account for differences in baryon fraction (see text for details). The square symbols are individual cluster Y_{500} values from the FO model and the dashed line the best-fitting GO relation. The dot–dashed lines are best-fitting relations from Nagai (2006); the upper line corresponds to their non-radiative (AD) simulation and the lower line their run with CSF. Finally, the triple-dot–dashed lines are taken from Krause et al. (2012) for their restricted A and B samples (upper and lower lines, respectively).

(strong feedback) compensates for this by heating the gas to a higher temperature.

Krause et al. (2012) present results for two cluster samples, A and B, shown as the upper and lower triple-dot–dashed lines in the figure. Both samples were simulated with the same GADGET2 *N*-body/SPH code as used in this study but contained different assumptions for the gas physics. Sample A contained 39 clusters resimulated from a large parent volume, while sample B was a mass-limited sample of 117 objects, taken from a single simulation. While both samples are larger than in Nagai (2006) the number of massive clusters is still significantly smaller than in our FO sample. The two samples (we show results restricted to clusters with $M_{500} > 2 \times 10^{14}\,h^{-1}\,M_\odot$) compare well with ours once the different baryon fraction is scaled out. The normalization in both cases is within 10 per cent or so, although the slope is slightly flatter, a result that appears only marginally significant (the slope of sample B is 1.64 ± 0.03 compared with the FO slope of 1.69 ± 0.02).

4.5 Comparison with observational data

We have also compared our results to observational data, now that blind SZ surveys are starting to yield significant numbers of (SZ-selected) clusters, enabling estimates of the Y_{500}–M_{500} relation to be performed (PXMM; Andersson et al. 2011). Here, we compare our results with those from the Planck Collaboration (PXMM), although we note that their best-fitting Y_{500}–M_{500} relation is similar to the SPT result derived from a lower number of clusters by Andersson et al. (2011).

The PXMM sample consists of 62 clusters with $z < 0.5$ and used X-ray data from *XMM–Newton* to define the size (r_{500}) and mass (M_{500}) of each cluster, calibrated using the X-ray M_{500}–$Y_{X,500}$ relation previously derived by Arnaud et al. (2010). Once the cluster size was defined, the SZ flux was measured using a multifrequency matched-filter technique, based on the ICM pressure profile of Arnaud et al. (2010). We show their best-fitting results to the Y_{500}–M_{500}, Y_{500}–$M_{gas,500}$ and Y_{500}–T_{sl} relations as the dashed lines and illustrate their intrinsic scatter with the boxes, in Figs 8–12. (Note we show these in both panels to help gauge the sense of evolution in our simulated relations, but the observed fits are more applicable to our $z = 0$ results.)

It is remarkable how well the PXMM results agree with our PC and FO models; only the Y_{500}–T_{sl} relation shows any obvious offset but that is nevertheless small. The reason for such good agreement is not obvious or necessarily expected, given the complicated procedure involved in deriving the observed parameters (we are using the simplest form of the simulated Y_{500}–M_{500} relation here).

Another interesting result from the PXMM sample is that the results are consistent with $Y_{500} = Y_{X,500}$ on average (again like our PC and FO models); however, the scatter in the observed relation is significantly larger than ours (observationally, $\sigma_{\log_{10} Y} = 0.1$, around a factor of 5 larger than for our PC and FO simulations). As a result, the scatter in the other observed PXMM scaling relations is also larger than ours; for example, the scatter is two to three times larger for the Y_{500}–M_{500} relation. Thus, if our PC and FO simulations, calibrated to X-ray data, provide faithful estimates of the mean SZ/X-ray scaling relations, observational estimates of the quantities must somehow increase the scatter without introducing significant bias. One potential source of scatter is due to the projection of large-scale structure along the line of sight; we investigate this below.

4.6 Projection effects

As detailed in Section 2.6 we have constructed 50 5 × 5-deg^2 mock realizations of the SZ sky (Compton-y maps) from our GO and PC simulations. (Unfortunately, it is not currently possible to do this for the FO model as it was not run on the full Millennium volume.) We use these maps to estimate the (cylindrical) Y_{500} for the clusters that are present, as follows.

First, we cross-match our 50 maps with cluster catalogues at all available redshifts (catalogues are constructed for all snapshots used to make the maps, provided there are objects above our mass limit of $M_{500} = 10^{14}\,h^{-1}\,\mathrm{M}_\odot$). This is done by performing the same operations (translation, rotation, reflection) on the cluster centre coordinates as was done with each of the snapshots, then finding the pixel in the map that corresponds to the cluster centre, for those objects within the map region. We then identify which pixels fall within the projected radius, $R_{500} = r_{500}$, and compute the SZ Y_{500} value which we define as

$$Y_{500}^{\mathrm{sky}} = D_{\mathrm{A}}^2\,\delta\Omega \sum_{i,j} y_{i,j}, \tag{18}$$

where the sum is performed over all relevant pixels (with indices, i, j) and $\delta\Omega$ is the solid angle of each pixel (we use 1200 × 1200 pixels so assume $\delta\Omega = 0.25 \times 0.25$ arcmin^2). Finally, we throw away clusters that have a more massive neighbour whose centre lies within its own radius, R_{500}, as this interloper would dominate the estimated SZ flux. Our final catalogue is restricted to clusters with $M_{500} > 10^{14}\,h^{-1}\,\mathrm{M}_\odot$ and $z < 1$; for comparative purposes, we split this into a low-redshift ($z < 0.5$) and a high-redshift ($z > 0.5$) subsample. The number of clusters in each of these sub-samples for the GO and PC models is listed in Table 4. The larger numbers in the high-redshift sample are expected due to the larger volume there (for fixed solid angle). Note that the same cluster could appear more than once (in a different realization or redshift).

In order to extract the cluster signal from the rest of the large-scale structure along the line of sight, we also compute cylindrical Y_{500} values due to the cluster region itself. To do this, we apply equation (18) to our cluster maps, detailed in Section 2.5. As a reminder, the length of the cylinder, centred on the cluster, is $z = 12r_{500}$; this approximately corresponds to three virial radii from the centre in each direction along the line of sight. We refer to this Y value as Y_{500}^{clus}; clearly $Y_{500}^{\mathrm{sky}} > Y_{500}^{\mathrm{clus}}$ by definition.

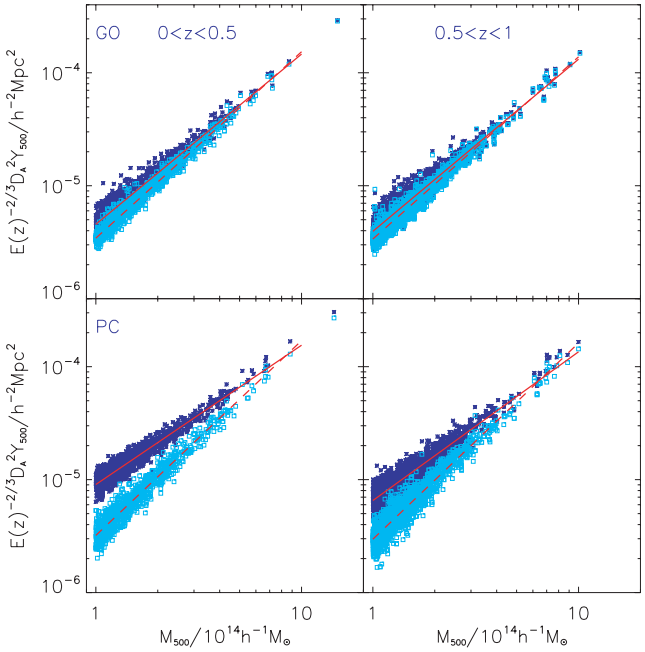

Figure 15. Projected Y_{500}–M_{500} relations for clusters in the GO (top panels) and PC (bottom panels) sky maps with $0 < z < 0.5$ (left-hand panels) and $0.5 < z < 1$ (right-hand panels). The stars correspond to Y_{500}^{sky} values, that is, calculated from the full sky map. The squares correspond to Y_{500}^{clus} values, that is, from the cluster region. In both cases the true M_{500} values were used. The dashed line is a best fit to the Y_{500}^{clus}–M_{500} relation and the solid line to the Y_{500}^{sky}–M_{500} relation. The Y_{500}^{sky} values are higher on average than Y_{500}^{clus}, especially in the PC simulation at low mass and low redshift, where the difference is a factor of 2–3.

The squares in Fig. 15 represent the Y_{500}^{clus}–M_{500} relation for our GO (top panels) and PC (bottom panels) models at high (left-hand panels) and low (right-hand panels) redshifts. We rescale cluster Y_{500}^{clus} values by $E(z)^{-2/3}$ to account for evolution across the redshift range in each panel. Best-fitting parameters (A, B, $\sigma_{\log Y}$) are given

Table 4. Best-fitting parameters for simulated SZ scaling relations using projected (cylinder) values from cluster and sky maps (see text for further details). Column 1 gives the scaling relation being considered; column 2 the redshift range; column 3 the simulation model; column 4 the number of clusters used in the fit; columns 5 and 6 list the best-fitting values for the normalization and slope parameters, respectively; and column 7 lists the estimated scatter in $\sigma_{\log_{10} Y}$. Quoted uncertainties correspond to either the 16th or 84th percentile (whichever is largest), estimated using the bootstrap resampling technique.

Flux	Redshift	Model	N_{clus}	A	B	$\sigma_{\log_{10} Y}$
Y_{500}^{clus}–M_{500}	$0 < z < 0.5$	GO	1346	-4.677 ± 0.003	1.650 ± 0.007	0.045 ± 0.001
		PC	1074	-4.671 ± 0.004	1.72 ± 0.01	0.068 ± 0.002
	$0.5 < z < 1$	GO	2952	-4.702 ± 0.002	1.613 ± 0.007	0.050 ± 0.001
		PC	2199	-4.699 ± 0.003	1.74 ± 0.01	0.077 ± 0.001
Y_{500}^{sky}–M_{500}	$0 < z < 0.5$	GO	1346	-4.622 ± 0.003	1.507 ± 0.009	0.059 ± 0.001
		PC	1074	-4.455 ± 0.003	1.23 ± 0.01	0.059 ± 0.001
	$0.5 < z < 1$	GO	2952	-4.677 ± 0.003	1.524 ± 0.007	0.062 ± 0.001
		PC	2199	-4.556 ± 0.003	1.32 ± 0.02	0.071 ± 0.001
$Y_{500}^{\mathrm{skysub}}$–$M_{500}$	$0 < z < 0.5$	GO	1346	-4.686 ± 0.004	1.71 ± 0.01	0.074 ± 0.003
		PC	1074	-4.683 ± 0.005	1.80 ± 0.02	0.106 ± 0.003
	$0.5 < z < 1$	GO	2952	-4.719 ± 0.003	1.666 ± 0.009	0.071 ± 0.001
		PC	2199	-4.721 ± 0.004	1.80 ± 0.01	0.104 ± 0.002

in Table 4; a pivot mass of $3 \times 10^{14}\,h^{-1}\,\mathrm{M}_{\odot}$ was adopted for all the fits. The GO model relations show similar trends to those seen in the spherical Y_{500}–M_{500} relation; the slope is close to self-similar and the scatter is small. The PC relations again have slopes that are steeper than the self-similar value but also have slightly larger scatter ($\sigma_{\log_{10} Y} \simeq 0.07$–$0.08$), reflecting in part the effect of additional evolution with redshift.

The stars in Fig. 15 are for when Y_{500}^{sky} values are used and thus contain the additional signal from beyond the cluster. The difference between the two relations in each panel (as can be seen from the best-fitting lines) is most prominent for the PC model, where the slope has decreased from ∼1.7 to ∼1.2, due to Y_{500}^{sky} being significantly larger than Y_{500}^{clus} in the lower mass objects. As was discussed in Section 2, the preheating was applied everywhere at $z = 4$ and thus substantially increased the thermal energy of the gas, as indicated by the three-fold increase in the mean y signal. Such widespread heating is likely to be unrealistic as it would require a huge amount of energy and would boil off the small amount of neutral hydrogen and helium in the IGM (Theuns et al. 2001; Borgani & Viel 2009), so the PC result represents a worse-case scenario for the effects of projection on the Y signal.

Observations of the SZ effect made with the *Planck* satellite are unable to measure the mean y signal as at each frequency, spatial temperature fluctuations are measured with respect to the all-sky mean. It is therefore more realistic to compare the *background-subtracted* values of Y_{500}^{sky} to the cluster values. To do this we compute the projected angular area for each cluster and compute the expected contribution to Y_{500} from the mean y:

$$Y_{500}^{\mathrm{skysub}} = Y_{500}^{\mathrm{sky}} - \langle y \rangle\, D_{\mathrm{A}}^2\, \Omega_{500}, \tag{19}$$

where Ω_{500} is the solid angle subtended by the cluster out to a projected radius, R_{500}. The results of this procedure are shown in Fig. 16, with best-fitting parameters for the $Y_{500}^{\mathrm{skysub}}$–$M_{500}$ relations given in Table 4.

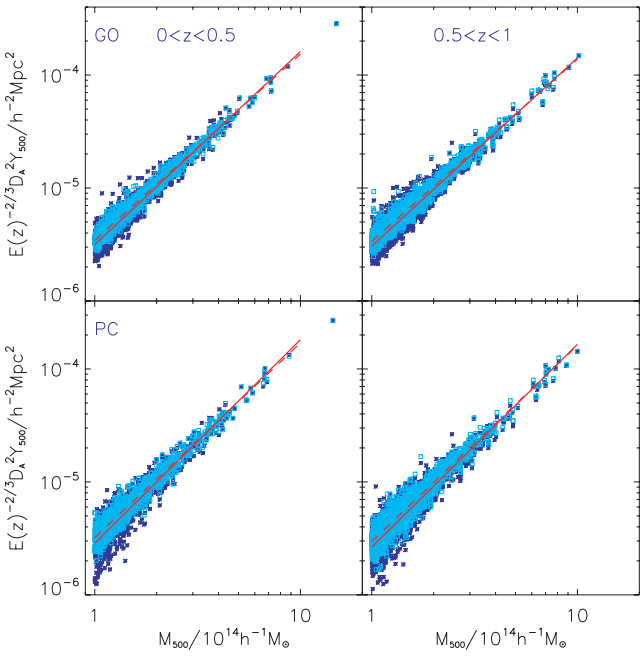

Figure 16. As in Fig. 15 but the Y_{500}^{sky} values have had the mean background signal subtracted. The two best-fitting relations are now very similar in all panels.

Interestingly, the two best-fitting relations are now almost identical for each run and within each redshift range. A simple background subtraction therefore removes any bias in the mean relation generated from the additional hot gas along the line of sight. The scatter is considerably larger in the $Y_{500}^{\mathrm{skysub}}$–$M_{500}$ relation, in part due to the fact that the additional signal is not constant everywhere. The PC relations again contain the largest scatter, comparable to the observed scatter in the PXMM data ($\sigma_{\log_{10} Y} \simeq 0.1$). Although the result is model-dependent, it is clear that part (if not all) of the observed scatter can be attributed to projection effects.

5 HYDROSTATIC BIAS

In the previous section, we saw that our PC and FO models produced SZ/X-ray scaling relations that were in good agreement with the PXMM observational data. A significant uncertainty in the observational determination of scaling relations is the (direct or indirect) assumption of HSE, required for deriving the cluster mass (M_{500}) and radius (r_{500}). It is therefore interesting to look at the accuracy of this assumption in our simulations as the good agreement between our results and the observations can only be preserved if hydrostatic bias is small (in the absence of additional systematic effects).

For a cluster in HSE, the pressure gradient in the ICM is sufficient to balance gravity; the total mass of the cluster can then be calculated as

$$M^{\mathrm{HSE}}(< r) = -\frac{kTr}{G\mu m_{\mathrm{H}}} \left(\frac{\mathrm{d}\ln\rho}{\mathrm{d}\ln r} + \frac{\mathrm{d}\ln T}{\mathrm{d}\ln r} \right), \tag{20}$$

where $\mu = 0.59$ is the mean molecular weight for an ionized plasma (assuming zero metallicity). We use the spectroscopic-like temperature to evaluate the local temperature, $T(r)$, and its gradient, $\mathrm{d}\ln T/\mathrm{d}\ln r$, at radius r.

Estimation of the cluster mass based on HSE can be biased for three reasons. First, the estimated mass within a fixed radius can be different from the true mass because the intracluster gas is not perfectly hydrostatic. Previous simulations have shown that mass estimates can be too low by up to 20 per cent, due to incomplete thermalization of the gas (e.g. Evrard, Metzler & Navarro 1996; Kay et al. 2004; Rasia, Tormen & Moscardini 2004; Rasia et al. 2006; Kay et al. 2007; Nagai, Vikhlinin & Kravtsov 2007a; Nagai et al. 2007b; Piffaretti & Valdarnini 2008; Ameglio et al. 2009; Lau, Kravtsov & Nagai 2009). A second effect is that the X-ray temperature of the gas may be lower than the mean (mass-weighted) temperature. Such an effect depends on the thermal structure of the gas (in particular, the low-entropy tail associated with substructure) and can be particularly severe when radiative cooling effects are strong.[6] Finally, the cluster's size itself is usually defined as a scale radius (e.g. r_{500}) which is mass-dependent so also depends on the assumption of HSE.

To study how these combined effects impact upon our scaling relations, we estimate the hydrostatic mass of each cluster as follows. First, we compute the hot gas ($T > 10^5$ K) density and temperature profiles. In lower mass clusters, the profiles can get rather noisy due to limited particle numbers which can affect the estimation of the pressure gradient. To avoid this, we fit a cubic polynomial function to each profile (in log-space) to generate a smoothed representation. (This also has the advantage that the gradient can be

[6] We note that Nagai et al. (2007a) found the X-ray temperature to be higher than the mass-weighted temperature in a mock *Chandra* analysis of their simulated clusters, but they exclude any resolved cold clumps from their calculation.

Table 5. Best-fitting parameters for simulated SZ scaling relations, with estimated properties from the assumption of HSE. Column 1 gives the scaling relation being considered; column 2 the redshift; column 3 the simulation model; column 4 the number of clusters used in the fit; columns 5 and 6 list the best-fitting values for the normalization and slope parameters, respectively; and column 7 lists the estimated scatter in $\sigma_{\log_{10} Y}$ or $\sigma_{\log_{10} M}$ (whichever is appropriate). Quoted uncertainties correspond to either the 16th or 84th percentile (whichever is largest), estimated using the bootstrap resampling technique.

Relation	Redshift	Model	$N_{\rm clus}$	A	B	$\sigma_{\log_{10} Y}/\sigma_{\log_{10} M}$
$E(z)^{-2/3}Y_{500}^{\rm HSE}$–$M_{500}^{\rm HSE}$	$z=0$	GO	439	-4.54 ± 0.02	1.60 ± 0.07	0.186 ± 0.008
		PC	738	-4.75 ± 0.009	1.69 ± 0.03	0.111 ± 0.005
		FO	179	-4.69 ± 0.01	1.50 ± 0.05	0.13 ± 0.01
	$z=1$	GO	25	-4.6 ± 0.3	1.6 ± 0.8	0.21 ± 0.03
		PC	94	-4.96 ± 0.04	1.5 ± 0.1	0.11 ± 0.01
		FO	57	-4.76 ± 0.06	1.4 ± 0.2	0.14 ± 0.02
$E(z)^{2/5}M_{500}^{\rm HSE}$–$Y_{X,500}^{\rm HSE}$	$z=0$	GO	787	0.44 ± 0.01	0.58 ± 0.02	0.118 ± 0.004
		PC	672	0.571 ± 0.007	0.545 ± 0.009	0.064 ± 0.003
		FO	179	0.57 ± 0.01	0.60 ± 0.02	0.080 ± 0.007
	$z=1$	GO	98	0.37 ± 0.06	0.50 ± 0.07	0.13 ± 0.01
		PC	86	0.69 ± 0.03	0.57 ± 0.04	0.066 ± 0.008
		FO	74	0.56 ± 0.02	0.59 ± 0.04	0.09 ± 0.01
$E(z)^{-2/3}Y_{500}^{Y_{\rm X}}$–$M_{500}^{Y_{\rm X}}$	$z=0$	GO	398	-4.356 ± 0.009	1.84 ± 0.02	0.055 ± 0.002
		PC	736	-4.694 ± 0.001	1.840 ± 0.004	0.0150 ± 0.0005
		FO	175	-4.668 ± 0.002	1.659 ± 0.008	0.019 ± 0.001
	$z=1$	GO	31	-4.29 ± 0.03	2.09 ± 0.09	0.052 ± 0.007
		PC	102	-5.040 ± 0.002	1.757 ± 0.005	0.0092 ± 0.0008
		FO	75	-4.799 ± 0.004	1.67 ± 0.02	0.022 ± 0.006

derived analytically.) We then use these model profiles to estimate the mass, $M^{\rm HSE}$, using equation (20), then vary the radius, r, until the following equation is satisfied:

$$M_{500}^{\rm HSE} = \frac{4\pi}{3}\left(r_{500}^{\rm HSE}\right)^3 500\rho_{\rm cr}(z), \qquad (21)$$

where $M_{500}^{\rm HSE}$ and $r_{500}^{\rm HSE}$ are our estimated mass and radius, respectively. Once the radius is known we can use this to estimate the SZ flux which we will denote by $Y_{500}^{\rm HSE}$. Again, this is the flux from within a sphere centred on the cluster; all that has changed is the assumed value of r_{500}. In what follows, we only consider the subset of clusters in the estimated mass range, $10^{14} < M_{500}^{\rm HSE} < 10^{15}\, h^{-1}\,{\rm M}_\odot$. The number of clusters is listed for each model and redshift in Table 5.

5.1 Effect of hydrostatic assumption on cluster mass

We quantify the effect of hydrostatic assumption on cluster mass by considering the distribution of the estimated-to-true mass ratio, $R_{\rm M} \equiv \log_{10}(M_{500}^{\rm HSE}/M_{500})$, for our models at $z = 1$ and 0. (Note that $R_{\rm M}$ directly measures the resulting shift along the logarithmic mass axis.) The results are shown in Fig. 17.

At $z = 0$, the GO results show a significant spread in mass ratios as well as a large negative bias; the median value is $R_{\rm M} = -0.14$. In the PC and FO models, the spread and bias is smaller, with the median increasing to around -0.05. A similar situation is evident at $z = 1$. The disturbed subsample, where HSE should definitely not be a good approximation, shows a small offset in the median $R_{\rm M}$ from the overall sample; in the PC and FO cases, the offset is positive, whereas in the GO case it is negative.

It is perhaps not surprising that the discrepancy between estimated and true mass from the GO simulation is significantly higher than for the PC and FO models. As is evident from the Y_{500}–$Y_{\rm X,500}$ relation (Fig. 13), the former model predicts a more clumpy ICM due to the

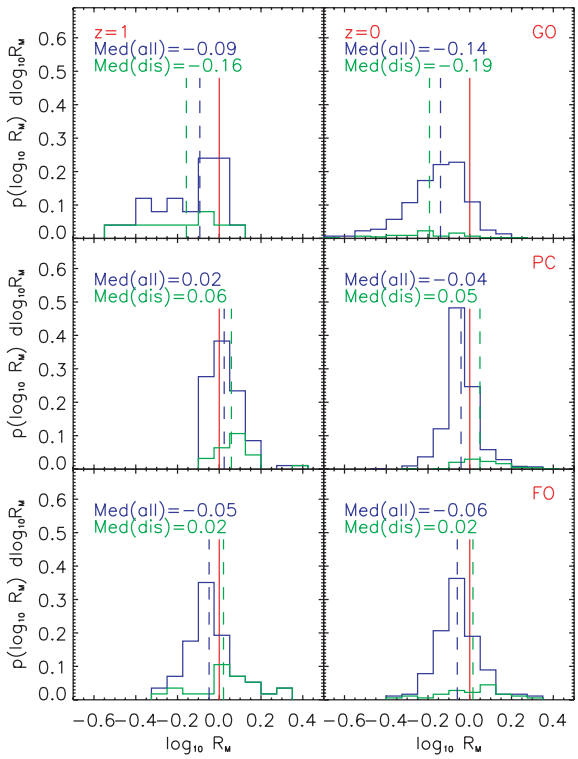

Figure 17. Distribution of estimated-to-true mass ratios, $R_{\rm M}$, within the estimated r_{500} for clusters at $z = 1$ (left-hand panels) and $z = 0$ (right-hand panels). The top panels show results from the GO model, middle panels from PC and bottom panels from FO. The green histogram is for the whole cluster sample, while the blue histogram is for the disturbed subsample. The vertical dashed lines indicate the median mass ratio for each case, with values given in the legend. The median $R_{\rm M}$ is significantly smaller in the runs with non-gravitational heating.

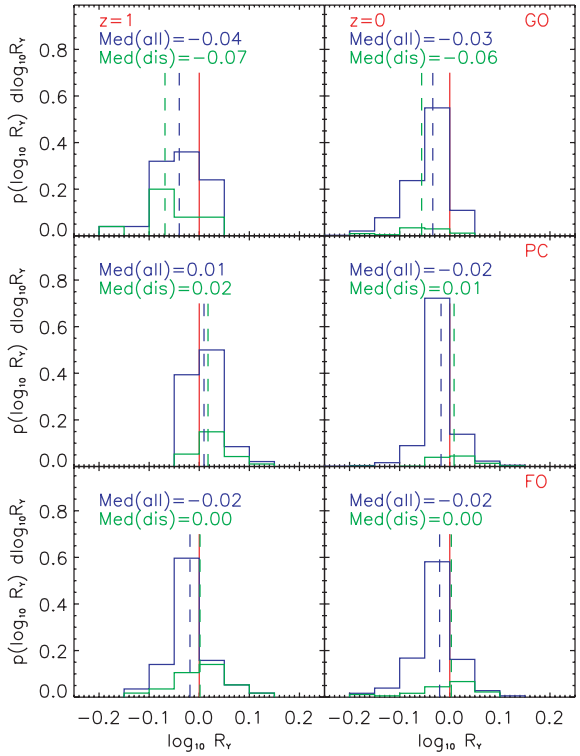

Figure 18. As in Fig. 17 but for the ratio of estimated-to-true Y_{500} values, $R_{\rm Y}$. The difference in $\log(Y_{500})$ is very small in the runs with non-gravitational heating.

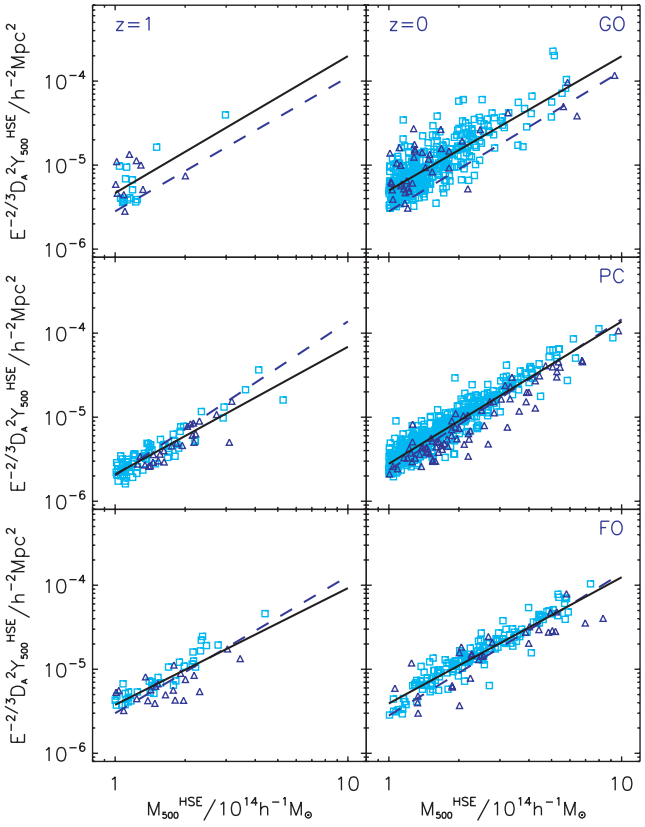

Figure 19. The $Y_{500}^{\rm HSE}$–$M_{500}^{\rm HSE}$ relations (i.e. using estimated values for each cluster assuming the gas is hydrostatic) for the GO, PC and FO models at $z = 1$ and 0. The squares correspond to regular clusters, while the triangles are disturbed clusters. The solid line is the best-fitting relation, while the dashed line shows the best-fitting true Y_{500}–M_{500} relation. Fits are performed for all clusters with $10^{14} < M_{500}^{\rm HSE} < 10^{15}\,h^{-1}\,{\rm M}_{\odot}$ and best-fitting parameter values are given in Table 5. It is clear that the hydrostatic assumption is more robust for the PC and FO runs than for the GO run.

persistence of low-entropy gas that is unable to cool. This gas by its very nature has not completely thermalized to the global cluster temperature and has significant residual bulk kinetic energy. In the latter two runs, the non-gravitational heating generates a smoother distribution which is evidently closer to HSE.

5.2 Effect of hydrostatic assumption on Y_{500} and $Y_{\rm X,500}$

The use of hydrostatic mass estimates also affects the SZ flux through the use of $r_{500}^{\rm HSE}$ to define the cluster radius; a smaller radius will result in a lower value for Y. We define a similar quantity to the mass ratio, $R_Y \equiv \log_{10}(Y_{500}^{\rm HSE}/Y_{500})$, and present the distribution of values in Fig. 18. Again, we present the ratio in this way as it directly gives the shift in $\log_{10}Y$ values due to the hydrostatic estimate.

As was the case with the total mass estimates, there is a larger bias (and scatter) in the Y_{500} values for the GO run, but the overall effect is smaller as it is entirely due to the (small) shift in r_{500}. The median R_Y is -0.03 for the GO run at $z = 0$, increasing to only -0.02 for the PC and FO runs. Since $r_{500}^{\rm HSE} < r_{500}$ on average, the integrated flux is also smaller. Again, the results are not significantly different at high redshift or when only the disturbed clusters are selected. We have also checked the equivalent result for the $Y_{\rm X,500}$ values and they are very similar to the Y_{500} results.

5.3 Estimated Y_{500}–M_{500} relation directly from HSE

We now put together these results to study how the Y_{500}–M_{500} relation is affected by hydrostatic assumption. These results are shown in Fig. 19 for the GO, PC and FO runs at $z = 1$ and 0. The best-fitting $Y_{500}^{\rm HSE}$–$M_{500}^{\rm HSE}$ relation is shown as a solid line and we also plot the best-fitting (true) Y_{500}–M_{500} relation as the dashed line in each panel. Values for the parameters describing the best-fitting relations (normalization, A; slope, B; and scatter, $\sigma_{\log_{10}Y}$) are given in Table 5.

The offset in M_{500} values ($R_{\rm M} = -0.14$ at $z = 0$) in the GO model is clearly visible in the top right-hand panel of Fig. 19, where the best-fitting relation is offset to larger Y_{500} values for a given value of $M_{500}^{\rm HSE}$. The large spread in the $R_{\rm M}$ distribution is also evident as the scatter has increased significantly ($\sigma_{\log_{10}Y} \simeq 0.19$, cf. Fig. 8 where $\sigma_{\log_{10}Y} \simeq 0.04$). The offset is insensitive to mass in this model, resulting in a relation that has similar slope (1.6) to the true Y_{500}–M_{500} relation. The offset in normalization has also led to a significant drop in the number of clusters in the sample at each redshift; as a result there are only 98 clusters at $z = 1$, making a reliable estimate of the relation difficult (but the trends are nevertheless consistent with those seen at $z = 0$).

The best-fitting $Y_{500}^{\rm HSE}$–$M_{500}^{\rm HSE}$ relation from the PC run at $z = 0$ is remarkably similar to the underlying relation, although the scatter has also increased considerably to $\sigma_{\log_{10}Y} \simeq 0.11$. Results at $z = 1$ prefer a flatter slope but this is somewhat affected by a few higher mass clusters (the slope is 1.5 ± 0.1). The estimated relation for the FO model is also similar to the true relation, with a preference for a slightly flatter slope and larger scatter ($\sigma_{\log_{10}Y} \simeq 0.13$ at $z = 0$). The disturbed cluster subsample is most strongly biased in the PC

results at $z = 0$, where the clusters have larger HSE masses for their flux, relative to the regular systems.

5.4 Estimated Y_{500}–M_{500} relation using $Y_{X,500}$

When mass estimates are required for larger samples of clusters, the direct hydrostatic method discussed above can be prohibitively expensive as it requires the density and temperature profiles to be known out to r_{500} and beyond. An alternative, indirect method is to use a mass *proxy*, where mass is estimated from a mass-observable scaling relation that is pre-calibrated using fewer clusters. Historically, T_X was the observable of choice but recent studies have focused on the use of Y_X due to its low scatter (Kravtsov et al. 2006; see also Arnaud, Pointecouteau & Pratt 2007; Maughan 2007; Arnaud et al. 2010; Sun et al. 2011). Indeed, the Planck Collaboration (PXMM) made use of the M_{500}–$Y_{X,500}$ relation, calibrated by Arnaud et al. (2010) from the REXCESS sample of 33 clusters, to estimate r_{500} and M_{500} for their larger (PXMM) sample of 62 clusters.

The procedure for estimating M_{500} works as follows. Assuming that all clusters lie on an M_{500}–$Y_{X,500}$ relation and that they evolve self-similarly with redshift, then r_{500} may be found using

$$r_{500}(Y_X) = \alpha\, E(z)^{-4/5}\, m(Y_X)^{1/3}\, h^{-1}\,\mathrm{Mpc}, \qquad (22)$$

where α is a known constant and $m(Y_X)$ is the best-fitting value of $E^{2/5}M_{500}(Y_{X,500})$ from the scaling relation for a given $Y_{X,500}$. The mass, $M_{500}(Y_X)$, can then be estimated using equation (21). In practice, this equation must be solved iteratively: a value for r_{500} is first guessed, then $Y_{X,500}$ is calculated within this radius (from the integrated gas mass and average X-ray temperature), allowing a new value for r_{500} to be computed from equation (22). This is repeated until convergence is achieved. Since clusters do not all lie on this relation (even though this particular relation is chosen for its low scatter), the derived r_{500} may be inaccurate for an individual cluster, but the overall relation should be unbiased.

We have applied this procedure to our simulated clusters and will refer to the resulting Y_{500}–M_{500} relation as the $Y_{500}^{Y_X}$–$M_{500}^{Y_X}$ relation. We first show our derived M_{500}^{HSE}–$Y_{X,500}^{HSE}$ relations, required for equation (22), for the three models at $z = 1$ and 0 in Fig. 20. Since Y_X (and not mass) is on the x-axis, we restrict our fits to clusters with $3 \times 10^{13} < Y_{X,500}^{HSE} < 10^{15}\, h^{-1}\,\mathrm{M}_\odot$ keV, as this approximately matches our adopted mass range (10^{14}–$10^{15}\, h^{-1}\,\mathrm{M}_\odot$) for the PC and FO models.

Qualitatively, the same conclusions can be drawn as for the Y_{500}^{HSE}–M_{500}^{HSE} relation (Fig. 19): the GO model shows a large scatter and the relation is offset due to the mass estimates being systematically low. As expected, however, the PC and FO results agree very well with the best-fitting underlying relation with still relatively small scatter, $\sigma_{\log_{10} M} = 0.06$–$0.08$. We also compare our results to the observed best-fitting relation at low redshift from Arnaud et al. (2010), shown as the dot–dashed line. The agreement between the PC and FO models is very good, with the latter preferring a slightly flatter slope than the observed relation.

The derived $Y_{500}^{Y_X}$–$M_{500}^{Y_X}$ relations are shown in Fig. 21. We have overlaid the best-fitting relation to these data (solid line); the best-fitting true Y_{500}–M_{500} relation (dashed line); the best-fitting Y_{500}^{HSE}–M_{500}^{HSE} relation (triple-dot–dashed line); and the best-fitting relation to the PXMM observational data (dot–dashed line).

The final result is very striking for our PC and FO models. At $z = 0$, there is only a small amount of bias (around 20 per cent or so, or $\Delta\log_{10} Y_{500} \simeq 0.08$) with respect to the underlying relation (and also, the PXMM relation). Such an offset, comparable to the estimated intrinsic scatter in the observed relation, is small enough that it may just reflect our method not exactly matching that used by the Planck Collaboration. Even more striking is the reduction in scatter; $\sigma_{\log_{10} Y} \simeq 0.02$ for the PC and FO models at $z = 0$, about half the size of the scatter in the true Y_{500}–M_{500} relation. The reason for this reduction is obvious: from Fig. 13 we saw that Y_{500} and $Y_{X,500}$ were strongly correlated, especially in the PC and FO models. Thus, a cluster that has a larger-than-average $Y_{X,500}$ for its mass will also have a larger-than-average Y_{500}. This was also true for the disturbed subsample, hence the reason why these clusters are unbiased with respect to the overall sample.

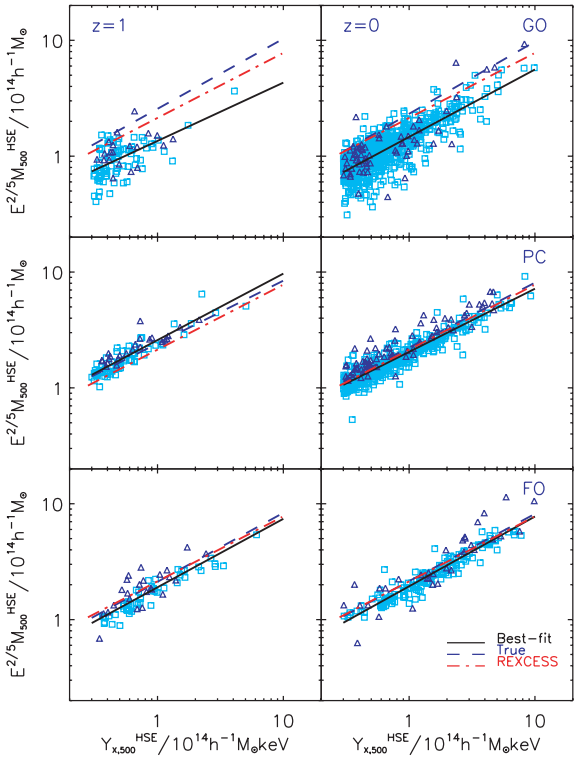

Figure 20. As in Fig. 19 but for the M_{500}^{HSE}–$Y_{X,500}^{HSE}$ relation. Clusters are now selected with $3 \times 10^{13} < Y_{X,500}^{HSE} < 10^{15}$ which, for the PC and FO models, matches well to our normal mass range. The solid line is the best fit to the relation and the dashed line the true relation. The dot–dashed line is the best-fitting relation from REXCESS (*XMM–Newton*) data as found by Arnaud et al. (2010).

6 SUMMARY AND CONCLUSIONS

Large surveys are now being performed at millimetre wavelengths exploiting the SZ effect to detect large samples of galaxy clusters out to high redshift. Such samples will then be used to produce competitive constraints on cosmological parameters, as well as to study the variation in physical properties of the intracluster gas (especially the gas pressure) with mass and redshift. The cosmological application relies on the statistical estimation of cluster mass through the SZ Y–M relation. In recent work (e.g. PXMM; Andersson et al. 2011) the first SZ-selected samples of clusters have already been used to estimate the cluster Y–M relation and full results of cosmological analyses are expected over the next few years.

In this paper, we have analysed some of the largest N-body/hydrodynamic simulations of structure formation (the MGSs) to study the dependence of SZ cluster properties on gas physics, at

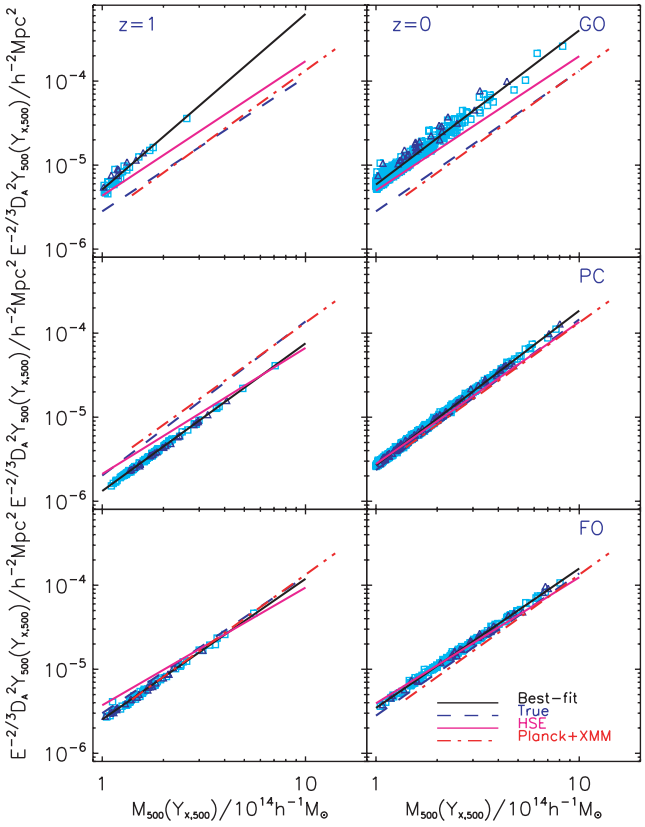

Figure 21. Y_{500}–M_{500} relations for the three models at $z = 1$ and 0 when r_{500}/M_{500} is estimated from the best-fitting $M_{500}^{\rm HSE}$–$Y_{\rm X,500}^{\rm HSE}$ relation with no scatter. We also show the best-fitting true Y_{500}–M_{500} relation (dashed line), the best-fitting $Y_{500}^{\rm HSE}$–$M_{500}^{\rm HSE}$ relation (triple-dot–dashed line) and the best-fitting $z < 0.5$ relation from PXMM data (PXMM; dot–dashed line). The PC and FO models agree well with the observational data although there is a slight offset. The scatter is much lower, however, due to the strong correlation between Y_{500} and $Y_{\rm X,500}$.

both low ($z = 0$) and high ($z = 1$) redshift. The large volume used in these simulations produces significant (hundreds to thousands) samples of clusters over the interesting range of cluster masses (10^{14}–$10^{15}\,h^{-1}\,{\rm M}_\odot$). We considered three cluster gas physics models: a non-radiative (gravitational-heating-only) simulation that ought to produce an approximately self-similar cluster population; and two simulations that incorporate additional non-gravitational heating (a model that uniformly preheats the gas at high redshift and a model that includes feedback from stars and AGNs in galaxies). The feedback model is our most realistic, in that it has already been shown to reproduce many of the scaling properties of X-ray clusters, especially those with non-cool cores (Short et al. 2010).

We started by investigating the hot gas pressure profiles of our simulated clusters and how they compare to the pressure profile advocated by Arnaud et al. (2010). We then compared our derived SZ scaling relations (between Y_{500} and total mass, hot gas mass, X-ray temperature and the X-ray analogue to the SZ Y parameter, $Y_{\rm X}$) with the recent observational results, in particular those obtained from a combined SZ+X-ray analysis performed by the Planck Collaboration. We also tested two of the key assumptions used in the observed analysis, namely that the mean Y_{500}–M_{500} relation is unaffected by the assumption that the gas is hydrostatic and by the presence of any other hot gas along the line of sight. Our main conclusions can be summarized as follows:

(i) In accordance with previous studies, our simulation with non-radiative hydrodynamics produces a (spherical) Y_{500}–M_{500} relation that has a self-similar slope (5/3) and also evolves with redshift according to the self-similar expectation, $E(z)^{2/3}$. Simulations with non-gravitational heating (both preheating and feedback cases) create slightly steeper Y_{500}–M_{500} relations (with a slope of 1.7–1.8, when clusters across the mass range $10^{14} < M_{500} < 10^{15}\,h^{-1}\,{\rm M}_\odot$ are considered), but the evolution with redshift is still close to self-similar.

(ii) The simulations were compared with the *Planck*+*XMM* results at $z < 0.5$ (PXMM) and very good agreement was found for a number of scaling relations (Y_{500} versus M_{500}, $M_{\rm gas,500}$ and $kT_{\rm X}$) for the preheating and feedback models. The scatter in the Y_{500}–M_{500} relation is smaller than observed, however, with $\sigma_{\log_{10} Y} \simeq 0.04$.

(iii) Intracluster gas in the non-radiative simulation contains a significant unthermalized component, due to the presence of low-entropy, clumpy gas. This causes an offset in the Y_{500}–$Y_{\rm X,500}$ relation, which tests the difference between the mass-weighted and X-ray temperatures. As a result, hydrostatic mass estimates are biased low by 20–30 per cent. The preheating and feedback simulations, on the other hand, predict smoother gas distributions, with $Y_{500} \simeq Y_{\rm X,500}$ and much smaller hydrostatic bias (estimated masses are only $\sim$10 per cent lower).

(iv) The estimated M_{500}–$Y_{\rm X,500}$ relations (assuming the gas is hydrostatic) are in good agreement with the recent observational determination by Arnaud et al. (2010). When $Y_{\rm X,500}$ is used as a mass proxy to predict the SZ Y_{500}–M_{500} relation, only a small ($\sim$20 per cent) offset in normalization from the true relation (and thus the observed relation from *Planck*+*XMM* data) is found. The scatter in the recovered relation is very small ($\sigma_{\log_{10} Y} \simeq 0.02$) due to the strong correlation between Y_{500} and $Y_{\rm X,500}$. Clusters that are undergoing major mergers are not significantly offset from the mean relation.

(v) Hot gas pressure profiles are well described by generalized NFW profiles, as suggested by Nagai et al. (2007b) and show that the majority of the contribution to the SZ Y parameter [where $r^3P(r)$ is maximal] comes from radii close to r_{500}. Splitting the cluster samples into low- and high-mass subsamples, we find little difference between the two in the run with non-radiative hydrodynamics, as expected. The runs with non-gravitational heating predict that low-mass clusters have lower core pressures and higher pressures in the cluster outskirts, when scaled according to the self-similar expectation. This non-self-similar behaviour can be attributed to the heating that is more effective in low-mass clusters and acts to push the gas out to large radii. There is also significant cluster–cluster scatter, especially in the core region and in the outskirts, where individual pressure profiles can be 50 per cent higher than the median profile.

(vi) We also compared our median pressure profiles with the Arnaud et al. profile and found good agreement (within 10 per cent) for our high-mass clusters at $r > 0.5r_{500}$, in the preheating and feedback models. Low-mass clusters are especially discrepant in the core regions, likely due to the absence of radiative cooling in our models. Using the X-ray temperature (rather than hot gas mass-weighted temperature) in the pressure calculation, as well as using hydrostatic estimates of r_{500} and M_{500}, only makes a significant ($>$10 per cent) difference to the non-radiative simulation for the reasons already mentioned.

(vii) Finally, we considered the effects of projection due to large-scale structure along the line of sight, by analysing 50 5 × 5-deg^2 maps of the thermal SZ effect. By measuring the cylindrical SZ flux associated with each cluster and comparing to the flux from the cluster region alone, we were able to discern the contribution

from additional structures, in the non-radiative and preheating simulations. The preheating model showed the largest bias, where low-mass clusters ($M_{500} \simeq 10^{14}\,h^{-1}\,\mathrm{M}_{\odot}$) had cylindrical Y_{500} values that were around two to three times higher than the value from the cluster region. This is due to the large amount of thermal energy injected into the gas at high redshift, as evidenced by the three-fold increase in the mean-y parameter. Subtracting the contribution from an assumed mean background we find the recovered Y_{500}–M_{500} relation to be unbiased with respect to the cluster relation, with some additional scatter that is model-dependent.

In summary, we can conclude that when our more realistic models for the intracluster gas are employed (namely those that raise the entropy of the gas to match global X-ray scaling relations), the SZ Y–M relation is in good agreement with the observations (Fig. 8) and is largely unaffected by two of the main sources of systematic uncertainty: hydrostatic bias (Figs 19 and 21) and projection effects from large-scale structure (Fig. 16).

While our analysis has been one of the most comprehensive to date and used some of the largest and most sophisticated simulation models, there are some significant shortcomings that still need to be addressed. First, the effects of radiative cooling were not included in our most realistic (feedback) model, so the model cannot yet match the full X-ray cluster population (namely the brightest objects with cool cores, Short et al. 2010). As we argued, this omission is likely not a significant problem for the Y–M relation but will affect the hot gas pressure profile so it should be addressed in future work. Secondly, we were unable to test projection effects for the feedback model as we only have a sample of clusters rather than the full cosmological volume. Finally, the cosmological model adopted for the simulations (identical to that used in the original MS) is no longer favoured; in particular, the value of σ_8 is higher than the current best estimate ($\sigma_8 = 0.9$ in the simulations, cf. $\sigma_8 \simeq 0.8$ from the *WMAP* 7-year data; Komatsu et al. 2011). Using the presently favoured cosmological model is likely to reduce the scale of projection effects, however, as in it structure formation will be less advanced.

We are currently preparing a new generation of MGSs that will rectify all of these problems, starting with a new version of our existing feedback model that will deal with the second and third issues. This new simulation, which is also being run at higher resolution and with an updated semi-analytic galaxy formation model (Guo et al. 2010), will additionally allow cosmologically-dependent statistical predictions for the SZ signal to be performed, namely the SZ power spectrum.

ACKNOWLEDGMENTS

We thank the reviewer, Stefano Borgani, for his insightful comments. The simulations used in this paper were performed at the University of Nottingham HPC Facility and on the ICC Cosmology Machine, which is part of the DiRAC Facility jointly funded by STFC, Large Facilities Capital Fund of BIS and Durham University. STK, MWP and RAB were supported by STFC through grant ST/G002592/1. CJS, PAT and ARL were supported by STFC through grants ST/F002858/1 and ST/I000976/1. OEY was supported by an STFC quota studentship.

REFERENCES

Aghanim N., de Luca A., Bouchet F. R., Gispert R., Puget J. L., 1997, A&A, 325, 9
Aghanim N., da Silva A. C., Nunes N. J., 2009, A&A, 496, 637
Allen S. W., Evrard A. E., Mantz A. B., 2011, ARA&A, 49, 409
Ameglio S., Borgani S., Pierpaoli E., Dolag K., Ettori S., Morandi A., 2009, MNRAS, 394, 479
Andersson K. et al., 2011, ApJ, 738, 48
Arnaud M., Pointecouteau E., Pratt G. W., 2007, A&A, 474, L37
Arnaud M., Pratt G. W., Piffaretti R., Böhringer H., Croston J. H., Pointecouteau E., 2010, A&A, 517, 92
Barbosa D., Bartlett J. G., Blanchard A., Oukbir J., 1996, A&A, 314, 13
Bartlett J. G., Silk J., 1994, ApJ, 423, 12
Battaglia N., Bond J. R., Pfrommer C., Sievers J. L., 2011, ApJ, submitted (arXiv:1109.3709)
Battye R. A., Weller J., 2003, Phys. Rev. D, 68, 083506
Benson B. A., Church S. E., Ade P. A. R., Bock J. J., Ganga K. M., Henson C. N., Thompson K. L., 2004, ApJ, 617, 829
Birkinshaw M., 1999, Phys. Rep., 310, 97
Birkinshaw M., Hughes J. P., 1994, ApJ, 420, 33
Bonaldi A., Tormen G., Dolag K., Moscardini L., 2007, MNRAS, 378, 1248
Bonamente M., Joy M., LaRoque S. J., Carlstrom J. E., Nagai D., Marrone D., 2008, ApJ, 675, 106
Borgani S., Viel M., 2009, MNRAS, 392, L26
Bower R. G., McCarthy I. G., Benson A. J., 2008, MNRAS, 390, 1399
Bryan G. L., Norman M. L., 1998, ApJ, 495, 80
Carlstrom J. E., Holder G. P., Reese E. D., 2002, ARA&A, 40, 643
Cole S., Kaiser N., 1988, MNRAS, 233, 637
da Silva A. C., Barbosa D., Liddle A. R., Thomas P. A., 2000, MNRAS, 317, 37
da Silva A. C., Kay S. T., Liddle A. R., Thomas P. A., Pearce F. R., Barbosa D., 2001, ApJ, 561, L15
da Silva A. C., Kay S. T., Liddle A. R., Thomas P. A., 2004, MNRAS, 348, 1401
De Lucia G., Blaizot J., 2007, MNRAS, 375, 2
Ebeling H., Edge A. C., Henry J. P., 2001, ApJ, 553, 668
Eke V. R., Cole S., Frenk C. S., 1996, MNRAS, 282, 263
Evrard A. E., Henry J. P., 1991, ApJ, 383, 95
Evrard A. E., Metzler C. A., Navarro J. F., 1996, ApJ, 469, 494
Fabjan D., Borgani S., Rasia E., Bonafede A., Dolag K., Murante G., Tornatore L., 2011, MNRAS, 416, 801
Fixsen D. J., Cheng E. S., Gales J. M., Mather J. C., Shafer R. A., Wright E. L., 1996, ApJ, 473, 576
Foley R. J. et al., 2011, ApJ, 731, 86
Golwala S. R. et al., 2009, Astro2010: The Astronomy and Astrophysics Decadal Survey, Science White Papers, no. 96
Guo Q., White S. D. M., Li C., Boylan-Kolchin M., 2010, MNRAS, 404, 1111
Hallman E. J., O'Shea B. W., Burns J. O., Norman M. L., arkness R., Wagner R., 2007, ApJ, 671, 27
Hartley W. G., Gazzola L., Pearce F. R., Kay S. T., Thomas P. A., 2008, MNRAS, 386, 2015
Huang C.-W. L. et al., 2010, ApJ, 716, 758
Jones M. et al., 1993, Nat, 365, 320
Kaiser N., 1986, MNRAS, 222, 323
Kaiser N., 1991, ApJ, 383, 104
Kay S. T., Liddle A. R., Thomas P. A., 1991, MNRAS, 325, 835
Kay S. T., Thomas P. A., Jenkins A., Pearce F. R., 2004, MNRAS, 355, 1091
Kay S. T., da Silva A. C., Aghanim N., Blanchard A., Liddle A. R., Puget J.-L., Sadat R., Thomas P. A., 2007, MNRAS, 377, 317
Kay S. T., Powell L. C., Liddle A. R., Thomas P. A., 2008, MNRAS, 386, 2110
Komatsu E. et al., 2011, ApJS, 192, 18
Krause E., Pierpaoli E., Dolag K., Borgani S., 2012, MNRAS, 419, 1766
Kravtsov A. V., Klypin A., Hoffman Y., 2002, ApJ, 571, 563
Kravtsov A. V., Vikhlinin A., Nagai D., 2006, ApJ, 640, 128
Lancaster K. et al., 2011, MNRAS, 418, 1441
Lau E. T., Kravtsov A. V., Nagai D., 2009, ApJ, 705, 1129
McCarthy I. G., Babul A., Holder G. P., Balogh M. L., 2003a, ApJ, 591, 515
McCarthy I. G., Holder G. P., Babul A., Balogh M. L., 2003b, ApJ, 591, 526
Marriage T. A. et al., 2011, ApJ, 737, 61

Maughan B. J., 2007, ApJ, 668, 772
Maughan B. J., Giles P. A., Randall S. W., Jones C., Forman W. R., 2012, MNRAS, 421, 1583
Mazzotta P., Rasia E., Moscardini L., Tormen G., 2004, MNRAS, 354, 10
Mehrtens N. et al., 2011, MNRAS, preprint (arXiv:1106.3056)
Menanteau F. et al., 2012, ApJ, 748, 7
Morandi A., Ettori S., Moscardini L., 2007, MNRAS, 379, 518
Motl P. M., Hallman E. J., Burns J. O., Norman M. L., 2005, ApJ, 623, L63
Nagai D., 2006, ApJ, 650, 538
Nagai D., Vikhlinin A., Kravtsov A. V., 2007a, ApJ, 655, 98
Nagai D., Kravtsov A. V., Vikhlinin A., 2007b, ApJ, 668, 1
Navarro J. F., Frenk C. S., White S. D. M., 1997, ApJ, 490, 493 (NFW)
Piffaretti R., Valdarnini R., 2008, A&A, 491, 71
Ade P. A. R. (Planck Collaboration) et al., 2011a, A&A, 536, A8
Ade P. A. R. (Planck Collaboration) et al., 2011b, A&A, 536, A9
Ade P. A. R. (Planck Collaboration) et al., 2011c, A&A, 536, A11 (PXMM)
Ade P. A. R. (Planck Collaboration) et al., 2011d, A&A, 536, A26
Poole G. B., Babul A., McCarthy I. G., Fardal M. A., Bildfell C. J., Quinn T., Mahdavi A., 2007, MNRAS, 380, 437
Press W. H., Schechter P., 1974, ApJ, 187, 425
Rasia E., Tormen G., Moscardini L., 2004, MNRAS, 351, 237
Rasia E. et al., 2006, MNRAS, 369, 2013
Romer A. K., Viana P. T. P., Liddle A. R., Mann R. G., 2001, ApJ, 2, 594
Rowley D. R., Thomas P. A., Kay S. T., 2004, MNRAS, 352, 508
Sehgal N. et al., 2011, ApJ, 732, 44
Shang C., Crotts A., Haiman Z., 2007, ApJ, 671, 136
Shaw L. D., Holder G. P., Bode P., 2008, ApJ, 686, 206
Shimwell T. W. et al. (AMI Consortium), 2011, preprint (arXiv:1101.5590)
Short C. J., Thomas P. A., 2009, ApJ, 704, 915
Short C. J., Thomas P. A., Young O. E., Pearce F. R., Jenkins A., Muanwong O., 2010, MNRAS, 408, 2213
Short C. J., Thomas P. A., Young O. E., 2012, MNRAS, preprint (arXiv:1201.1104)
Springel V., 2005, MNRAS, 364, 1105
Springel V., Hernquist L., 2002, MNRAS, 333, 649
Springel V. et al., 2005, Nat, 435, 629
Stanek R., Rudd D., Evrard A. E., 2009, MNRAS, 394, L11
Stanek R., Rasia E., Evrard A. E., Pearce F. R., Gazzola L., 2010, ApJ, 715, 1508
Staniszewski Z. et al., 2009, ApJ, 701, 32
Sun M., Sehgal N., Voit G. M., Donahue M., Jones C., Forman W., Vikhlinin A., Sarazin C., 2011, ApJ, 727, L49
Sunyaev R. A., Zel'dovich Y. B., 1972, Comments Astrophys. Space Phys., 4, 173
Theuns T., Mo H. J., Schaye J., 2001, MNRAS, 321, 450
Thomas P. A. et al., 1998, MNRAS, 296, 1061
Vanderlinde K. et al., 2010, ApJ, 722, 1180
Viana P. T. P. et al., 2012, MNRAS, in press (doi:10.1111/j.1365-2966.2012.20673.x) (arXiv:1109.1828)
Voit G. M., 2005, Rev. Mod. Phys., 77, 207
White M., Hernquist L., Springel V., 2002, ApJ, 579, 16
Wik D. R., Sarazin C. L., Ricker P. M., Randall S. W., 2008, ApJ, 680, 17
Williamson R. et al., 2011, ApJ, 738, 139
Yang H.-Y., Bhattacharya S., Ricker P. M., 2010, ApJ, 725, 1124
Young O. E., Thomas P. A., Short C. J., Pearce F., 2011, MNRAS, 413, 691

APPENDIX A: EVOLUTION OF SCALING RELATIONS

The following figures (Figs A1, A2 and A3) illustrate the evolution of the slope, normalization and scatter with redshift for the Y_{500}–$M_{\rm gas,500}$, Y_{500}–$T_{\rm sl}$ and Y_{500}–$Y_{\rm X,500}$ relations, respectively. Details of what is plotted in each panel are identical to Fig. 10 and are discussed in Section 4.2.

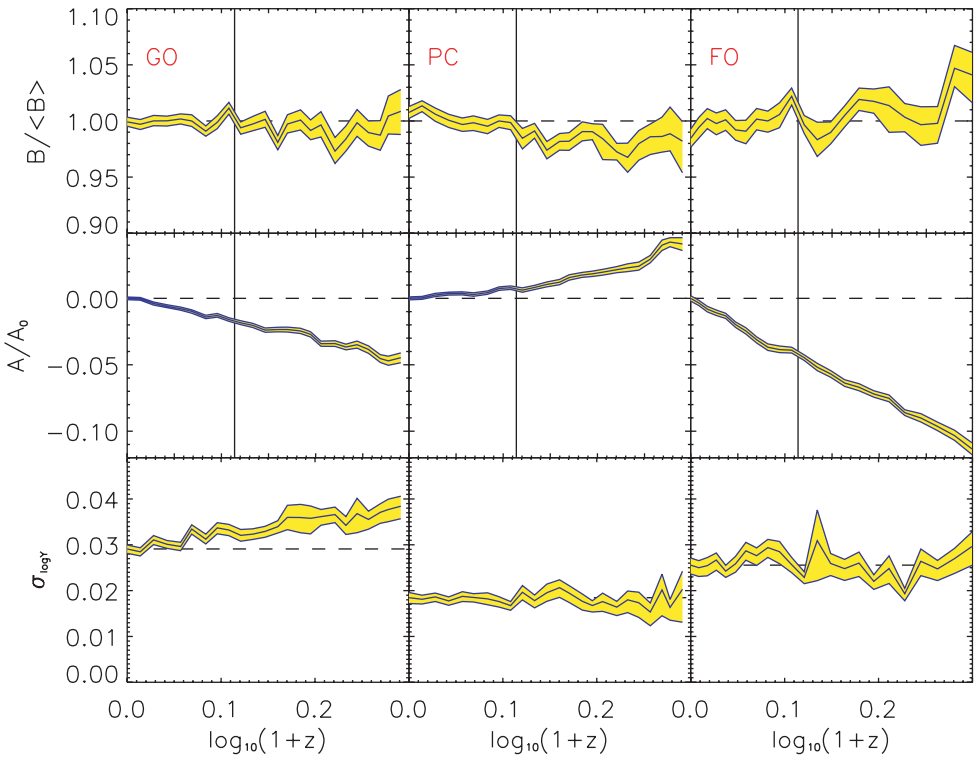

Figure A1. As in Fig. 10 but for the Y_{500}–$M_{\rm gas,500}$ relation.

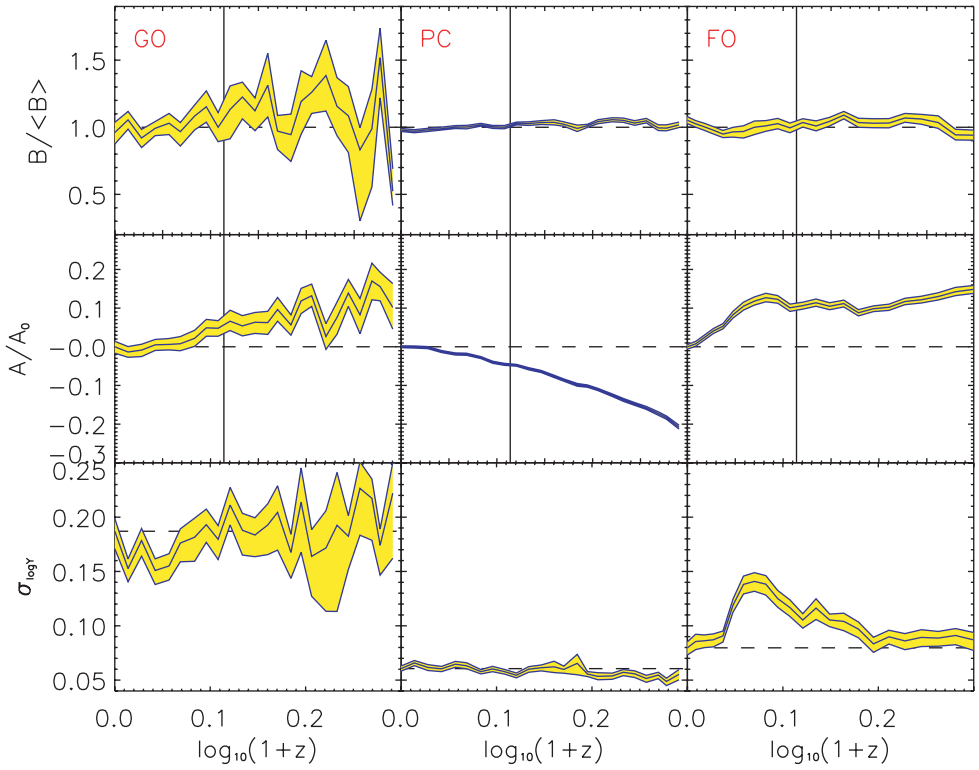

Figure A2. As in Fig. 10 but for the Y_{500}–T_{sl} relation.

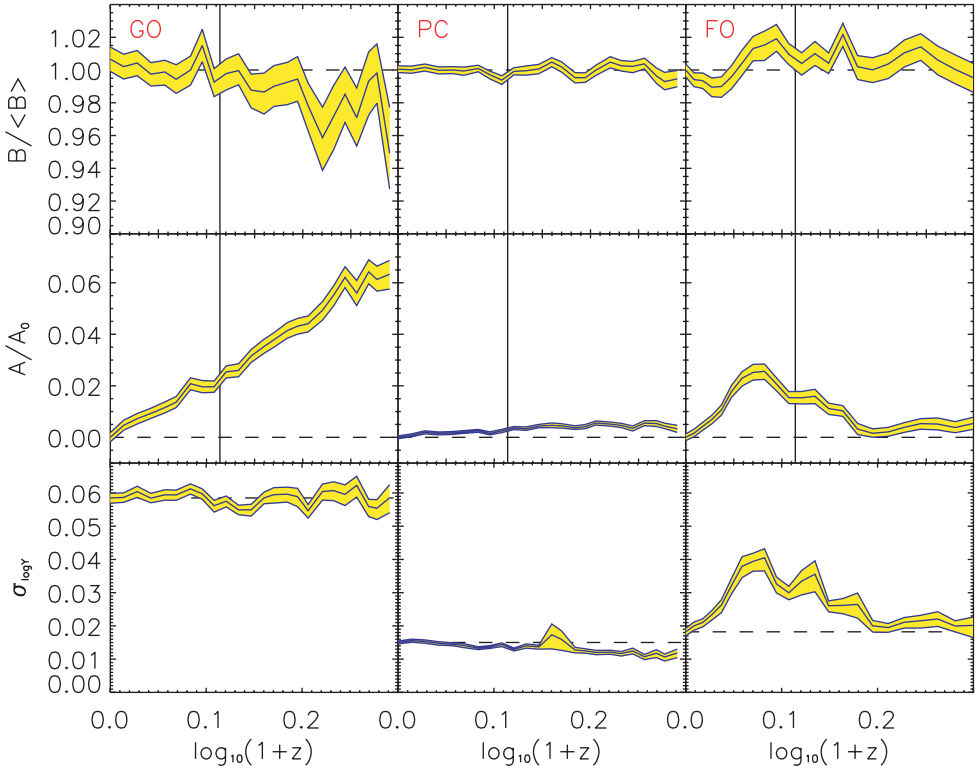

Figure A3. As in Fig. 10 but for the Y_{500}–$Y_{X,500}$ relation.

This paper has been typeset from a TEX/LATEX file prepared by the author.